Department of Materials Science and Technology, University of Crete

FORTH
INSTITUTE OF ELECTRONIC STRUCTURE AND LASER

TCMD
Transparent Conductive Materials & Devices Group

Perovskite semiconducting nanomaterials for hydrogen evolution

Vasiliki Faka

Supervisors
Dr. V. Binas
Prof. G. Kiriakidis

Master thesis Committee:
Prof. G. Armatas
Prof. I. Remediakis
Prof. C. Stoumpos

Heraklion, February 2021

Abstract

The aim of this master thesis is the synthesis and characterization of novel photocatalysts combined by metal titanate rods and carbon nitride nanosheets (CNNs), in order to be used for photocatalytic water splitting, under visible light for H_2 production. The metal titanate rods are ilmenite type materials ($MTiO_3$) with M = Co, Ni, Zn, Mg, which traditionally are not active photocatalysts for the H_2 production. The enormous advantages of transition metal titanates consist of their superior physicochemical properties, their low production cost, their simple and scalable synthesis and their low toxicity. These properties render them interesting to study as functional materials and attempt to develop them towards applications. Moreover, their tunable bandgap, their photo stability and their corrosion resistance in aqueous solutions make them good candidates for photocatalytic water splitting reactions. Therefore, the combination of transition metal titanates, with other, photoactive materials, such as CNNs, in order to make them active photocatalysts under visible light is the preferred method to exploit them. The emphasis of this master thesis is given to the synthetic procedure of the novel material and to the morphological, structural and optical properties. Therefore, all the synthesized powders were analyzed by powder X-Ray Diffractometry (PXRD), Scanning Electron Microscopy (SEM), Energy Dispersive X-Ray Spectroscopy (EDS) and UV-Vis-NIR spectroscopy. Finally, the powders were tested in photocatalytic water splitting for solar H_2 production, with the combination of metal titanates with CNNs to have increased the activity of the individual materials.

A

Acknowledgements

Dedicated to my family.

Table of Contents

Chapter 1 – Introduction

1.1 A brief overview on metal titanates

Metal titanates belong to a group of inorganic, functional materials that have been studied the last decades due to their easy synthetic procedure, good physiochemical properties and their wide range of applications. Metal titanates are compounds that contain a metal element, titanium and oxygen ions ($MTiO_3$) and have the structure of inorganic materials. The fundamental aspects for metal titanates had started to be established in 1950 and since then, titanates are investigating thoroughly due to their physiochemical properties. [1]

1.1.1 Synthetic strategies and applications of metal titanates

Since 1950, many research groups have been studying titanates synthesized by solid-state synthetic procedures. In the beginning, several studies were focused on the understanding of the phase transitions that occur in titanates by quenching, by changing the pressure or by changing the initial molar ratio of the materials in a process. [2] The main synthetic procedure used for the production of ilmenite materials was the traditional solid-state reaction method (SSR). [3] The main drawbacks of this method was the high sintering temperatures needed (usually above 1000 ^{o}C) and the long processing times. [4] In addition, the final materials produced by SSR, presented large particle sizes with limited degree of chemical homogeneity and high impurities. [5] Pure phase materials are beneficial to many applications – such as photocatalysis – because they reduce impurities and lead to fast charge transport from bulk to surface. [6] Therefore, the research interest was focused on searching new synthetic procedures in order to reduce these defects and to low the formation temperature of the crystals. Consequently, plenty of methods have been proposed due to their unique characteristics. One of these methods is a wet chemical method, the sol-gel technique; a process that takes place in mild conditions and can produce crystals with different shapes, sizes and morphology, but quite homogeneous and cost-effectively. [7] Another proposed wet chemical method is the stearic acid gel (SAG). Wang et al. in 2007 compared SAG with acetic acid gel method (AAG). The main drawbacks of AAG was the high crystalline formation temperature needed (800 ^{o}C) compared to SAG method, with which the nanopowder obtained at the intermediate temperature of 550 ^{o}C. In addition, Wang et al. observed that SAG method not only can decrease significantly the crystalline temperature, but also can prepare high purity nanopowders. [10],[11] Another method proposed in literature is the precipitation method followed by annealing. This method is regarded as simple because it can be performed in aqueous media and apart from maintaining the pH of the reaction; any other special equipment is not needed. [10] Another approach to prepare powders consisting of oxides of transition elements is the Pechini method. This procedure involves the dissolution of hydrous oxides or alkoxides of elements in a polyhydroxy alcohol with a chelating agent (such as citric acid) and by a thermal annealing of the powder at relative low temperatures, high homogeneity can be obtained. [11] All these methods are going to be analyzed in the following sections, by giving emphasis on the properties of the obtained materials.

1.1.1.1 Magnesium Titanate

The initial studies in literature for $MgTiO_3$ refer to the solid-state reaction technique using MgO and TiO_2 as the precursor materials in different molar ratios, which followed by a calcination at 1,500 °C. [2] In the studies reported the last years, researchers attempted to synthesize pure $MgTiO_3$ and found out that the reaction temperature and the initial concentration of the metal ions are two factors that affect the phase transformations in magnesium titanates. [6] In many studies, the mixed phases of $MgTiO_3$ are observed and research has been done in order to discover how they are affected by the calcination temperature. [12], [13], [14] However, it was a challenge to find novel routes for the synthesis of pure phase $MgTiO_3$ with narrow size distribution, using cheap raw materials. [12] Nanocrystalline magnesium titanate can be synthesized by a sol gel process followed by calcination at 700 °C, without the additional phases of Mg_2TiO_4, $MgTi_2O_5$ and TiO_2. [15] Pure single-phase $MgTiO_3$ flake-like nanocrystallites with well-defined particle morphology and a small particle size distribution can be synthesized by a stearic acid gel (SAG) method, with no impurities of other phases at a low temperature of 600 °C. [9] The reported methods in literature for the formation of pure $MgTiO_3$ include sonochemical method, [16] hydrothermal method, [17] sol-gel procedure [18] and electrospinning. [19] $MgTiO_3$ is transparent in the visible spectrum region and reveals a sharp absorption edge from 335 nm to 365 nm, namely a wide bandgap from 3.4 to 3.7 eV. It possesses a layered structure that facilitates the charge separation, high thermal and chemical stability [16] and has many industrial applications due to its dielectric properties in capacitors [20].

1.1.1.2 Zinc Titanate ($ZnTiO_3$)

In 1960, Dulin and Rase [21] made a fundamental analysis regarding the formation of $ZnTiO_3$ by setting up the phase diagram of ZnO-TiO_2 system. They found out that the phases of Zn_2TiO_4 and $ZnTiO_3$ are thermodynamically stable from 870 K (600 °C) and by increasing the temperature up to 1220 K (950 °C), $ZnTiO_3$ decomposes to form Zn_2TiO_4 and rutile TiO_2. One year later, Bartram and Slepetys showed for the first time $Zn_2Ti_3O_8$ – a metastable phase of zinc titanates which decomposes to form Zn_2TiO_4 and TiO_2. [22] In 1987, Yamaguchi et al. [23] studied the phase transformations of $ZnTiO_3$ in the system of ZnO-TiO_2. They clarified that $Zn_2Ti_3O_8$ is a low-temperature form of $ZnTiO_3$. They claimed that zinc orthotitanate Zn_2TiO_4 can be easily prepared by solid-state reaction between ZnO and TiO_2 in a 2:1 mole ratio. However, pure $ZnTiO_3$ cannot be produced from a mixture of ZnO:TiO_2, because $ZnTiO_3$ decomposes into Zn_2TiO_4 and TiO_2 (rutile) in the latter stages of the reaction, at about 945 °C. In their work, the starting temperature for the formation of zinc titanates, was at 600 °C and the cubic phase of $Zn_2Ti_3O_8$ appeared at 760 °C with a high intensity. The optimal temperature in order to produce hexagonal single phase $ZnTiO_3$ was at 965 °C, although this phase started to form at 820 °C. Therefore, 820 °C was the temperature that the cubic structure transformed to hexagonal. Then, the specimen heated up to 1100 °C and the phase of Zn_2TiO_4 and rutile were formed. Differential thermal analysis (DTA) was conducted in air (at a heating rate of 10 °C/min) and revealed the phase transformations of the sample during the annealing process. The DTA curve depicted in Figure 1, revealed an exothermic peak at 600 °C to 765 °C related to the phase transformation from cubic to

hexagonal phase and an endothermic peak at 965 ºC to 1010 ºC, resulted from the decomposition of $ZnTiO_3$ into Zn_2TiO_4 and TiO_2.
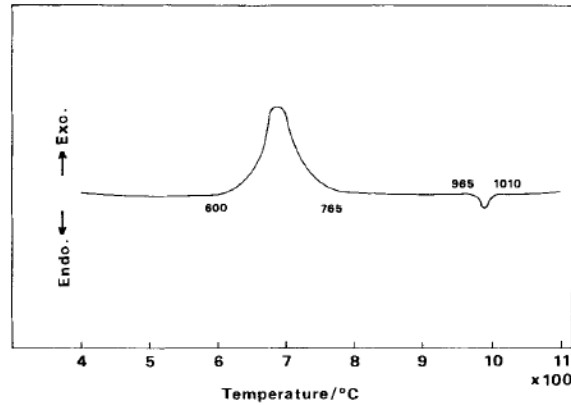
Figure 1. *DTA curve in ZnO-TiO₂ system.*

Budigi et al., proposed the chemical reactions taking place in zinc titanate system, during the increment of annealing temperature (see the following equations 1 to 5). [10]

$$3\,ZnTi(OH)_6 \xrightarrow{<400\,°C} Zn_2Ti_3O_8 \text{ (amorphous)} + ZnO \text{ (eq. 1)}$$

$$Zn_2Ti_3O_8 \text{ (amorphous)} + ZnO \xrightarrow{400\,°C\,-\,500\,°C} Zn_2Ti_3O_8(\text{cubic}) + ZnO \text{ (eq. 2)}$$

$$Zn_2Ti_3O_8 \text{ (cubic)} + ZnO \xrightarrow{600\,°C\,-\,700\,°C} 3\,ZnTiO_3 \text{ (cubic) (eq. 3)}$$

$$3\,ZnTiO_3 \text{ (cubic)} \xrightarrow{700\,°C\,-\,900\,°C} 2\,ZnTiO_3 \text{ (cubic)} + ZnTiO_3 \text{ (hexagonal) (eq. 4)}$$

$$2\,ZnTiO_3 \text{ (c)} + ZnTiO_3 \text{ (h)} \xrightarrow{>900\,°C} 1.5\,Zn_2TiO_4 \text{ (c)} + 1.5\,TiO_2 \text{ (rutile) (eq. 5)}$$
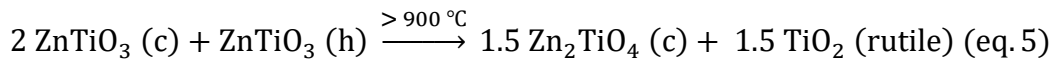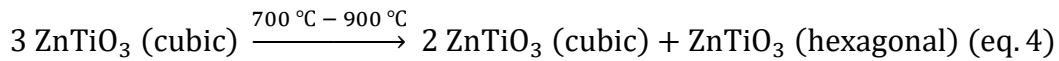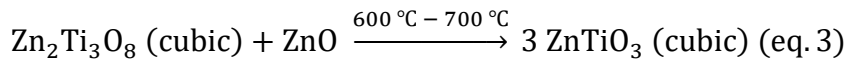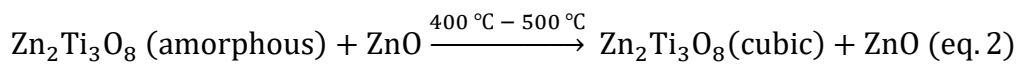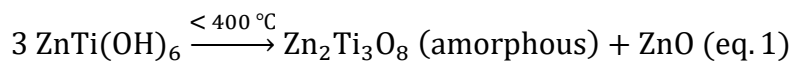
The reported techniques for the formation of $ZnTiO_3$ include the precipitation method, Pechini process[10], sol-gel method. [11] Based on the characteristics and properties of $ZnTiO_3$, the so far reported applications in literature include its usage as microwave resonator material, gas sensor (for ethanol, NO, CO), paint pigment and catalyst in liquid phase organic transformation, [11] dielectric ceramic, [24] sorbent for the desulfurization of hot coal gas, oxidative of hydrocarbons, CO and NO reduction. [10]

1.1.1.3 Nickel and Cobalt Titanate (NiTiO₃ and CoTiO₃)

The first mentions for nickel and cobalt titanates date back in 1960, when the initial studies reported the magnetic properties of these materials. [3] Since then, many studies have been published regarding the different synthetic procedures and applications, by giving emphasis in the morphological and structural properties. Rubinshtein et al. declared that NiO and TiO_2 do not form solid solutions and $NiTiO_3$ can not be formed below 1000 ºC. [25] Based on the general idea on synthesizing ilmenite materials, there have been published many works regarding the synthetic procedures and different morphologies obtained. These methods include the sol-gel process, [26],[27],[28] electrospinning, [29] pechini process, [30] and coprecipitation [31]. Their applications

include their usage as electrodes in solid oxide fuel cells, color mixtures of surface coating, sensors in gas sensing devices and hydrocarbonate catalyzers. [30]

1.1.2 Structural, electronic and optical properties of ilmenite $ATiO_3$

Metal titanates have the chemical formula $MTiO_3$, where M is a metal such as Mg, Bi, Fe, Co, Mn, Ni, Cu, Zn. Among these materials, the considered $MgTiO_3$, $ZnTiO_3$, $CoTiO_3$ and $NiTiO_3$ crystallize in the ilmenite structure, at room temperature under normal pressure and adopt an ordered corundum (Al_2O_3) and a hematite (Fe_2O_3) structure of hexagonal crystal system with a space group $R\bar{3}$ (no. 148) and C_{3i}^2 symmetry. [32] The ilmenite structure results from equal amounts of divalent (A^{2+}) and tetravalent (Ti^{4+}) cations ordered at the octahedral sites and alternate the c-axis of the unit cell. [4] Figure (2a) and (2b) describe the primitive cell of $CoTiO_3$ and $NiTiO_3$ ilmenite materials along c-axis, where as it seems the alternating layers of M and Ti atoms are perpendicular to c axis of the unit cell. Both cations M and Ti are octahedrally coordinated by oxygen. [32] Ti-O bonds possess the stronger covalent bonding strength than A-O bonds. It has been proved that the type of A-site ions does not affect the covalency of Ti-O bonds. [4]
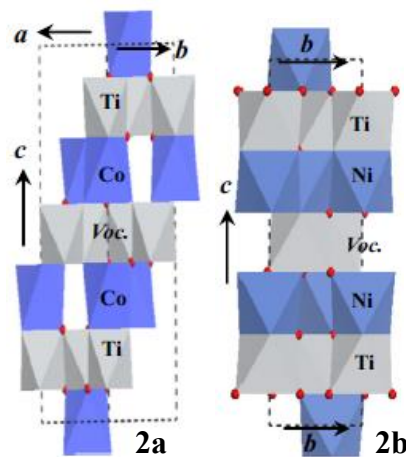
Figure 2. The primitive cells of (2a) CoTiO₃ and (2b) NiTiO₃ along c-axis are depicted.

The octahedral MO_6 and TiO_6 share their edges within each layer. More specifically, each metal octahedron (MO_6) shares three edges with the same metal octahedron in the same layer. The metal octahedron of the second type (TiO_6) belong to the adjacent layer and share a face with the metal octahedra of the previous layer along c-axis, a corner along the oblique direction and an opposite face with an empty octahedral site (Voc.) along c-axis. Along the a-axis, same type of octahedron structure shares an edge, adopting a AB-AB stacking motif. The arrangement for metal atoms and Ti atoms is – Ti–M–Vac–M–Ti– of face-shared pairs following a virtual pillar along the c-axis. [4], [32] In Figure 3, the primitive unit cell of some ilmenite materials is depicted in the terms of bonds, in order to be understood the covalent bond-structure that adopt each metal with oxygen atoms (M-O) and titanium with oxygen atoms (Ti-O). In addition, it is clear that each layer of cations connects with the previous or next layer with the peaks, through oxygen atoms. However, this representation is not helpful in order to understand the edge sharing, but only for the perspective of the covalent bonds that the

elements adopt. Titanium cations are represented with light blue atoms, metal cations are represented with grey atoms and oxygen atoms are represented with red colored atoms.
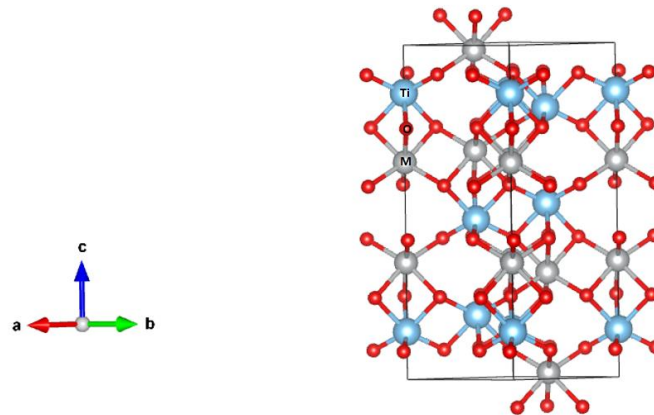
Figure 3. *The representation of primitive unit cells of ilmenite type with the view of element covalent bonding. The grey spheres belong to the metal cations, the blue spheres represent Titanium cations and the red spheres corresppond to oxygen ions.*

The Titanium centers in TiO_6 and Metal centers in MO_6 octahedron are subject to an octahedral crystal field in the crystal and thus, according to the crystal field theory, Ti-3d and M-3d orbitals split between t_{2g} (d_{xy}, d_{xz}, d_{yz}) and e_g (d_z^2, $d_{x^2-y^2}$) orbitals. The 3d orbitals of metal ions (3d-M and 3d-Ti) bond with the O-2p orbitals and form the molecular energy diagram depicted in Figure 4. The t_{2g} atomics orbitals contribute to the top of the valence band, while e_g atomic orbitals contribute to the bottom of the conduction band. The lower energy E_1 has derived from the non bonding orbitals O-2s. The E_2 energy has derived from the most stable bonding between the 3d-M with O-$2p_\sigma$ states and 3d-Ti with O-$2p_\sigma$ states. The E_3 energy belongs to the upper VB and is derived from the M-$3d_{yz}$ states combined with O-$2p_\pi$ states. The upper filled valence band is derived from the states O-$2p_\pi$, while the lowest and empty conduction band is dominated by the M-$3d_z^2$. The states of titanium are located in a higher energy in the conduction band, when the e_g orbitals of Ti interact with the e_g atomic orbitals of M derived from Ti-$3d_{x^2-y^2}$ and M-$3d_z^2$. [1], [32], [4]
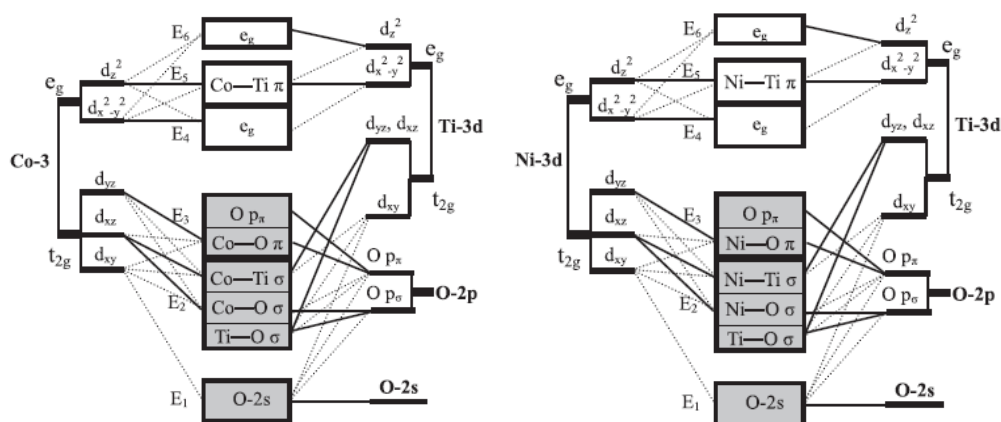
Figure 4. *Molecular orbital bonding diagram for (3a) $CoTiO_3$, (3b) $NiTiO_3$.*

In order to extend the comprehension of the molecular orbital diagram, the band structures of these materials are depicted in Figure 5. From these diagrams, it is clear that these semiconductors are indirect gap, because the minimum of the conduction band (CBM) is located at the K point and the corresponding valence band maximum (VBM) is located at the G point of the Brillouin zone. In addition, the band structures exhibit similar band distribution and energy regions in the ranges of VB and CB. Six different energies can be distinguished (E_1, E_2, E_3, E_4, E_5, E_6). These electronic compositions can be analyzed by the total densities of states (TDOS) and partial densities of states (PDOS). The lower VB (E_1) is derived from the O-2s states. The upper VB can be divided into two parts: the higher energy region derives from O-2p states with A-3d hybridized states and the second part derives from the O-2p states with involvement of Ti-3d states. The CB is derived from the A-3d states and Ti-3d states with a small amount of O-2p states. More specifically, the lower CB region is derived from the contribution of A-3d states, while the contribution of Ti-3d states is mainly situated in the higher energies (E_5, E_6). This model is in agreement with the molecular orbital schematic shown in Figure 4. Band structure calculations indicate that the $MTiO_3$ compounds possess an indirect bandgap, even though the exact value is greatly underestimated due to known inefficiency of DFT theory to predict it. [32]
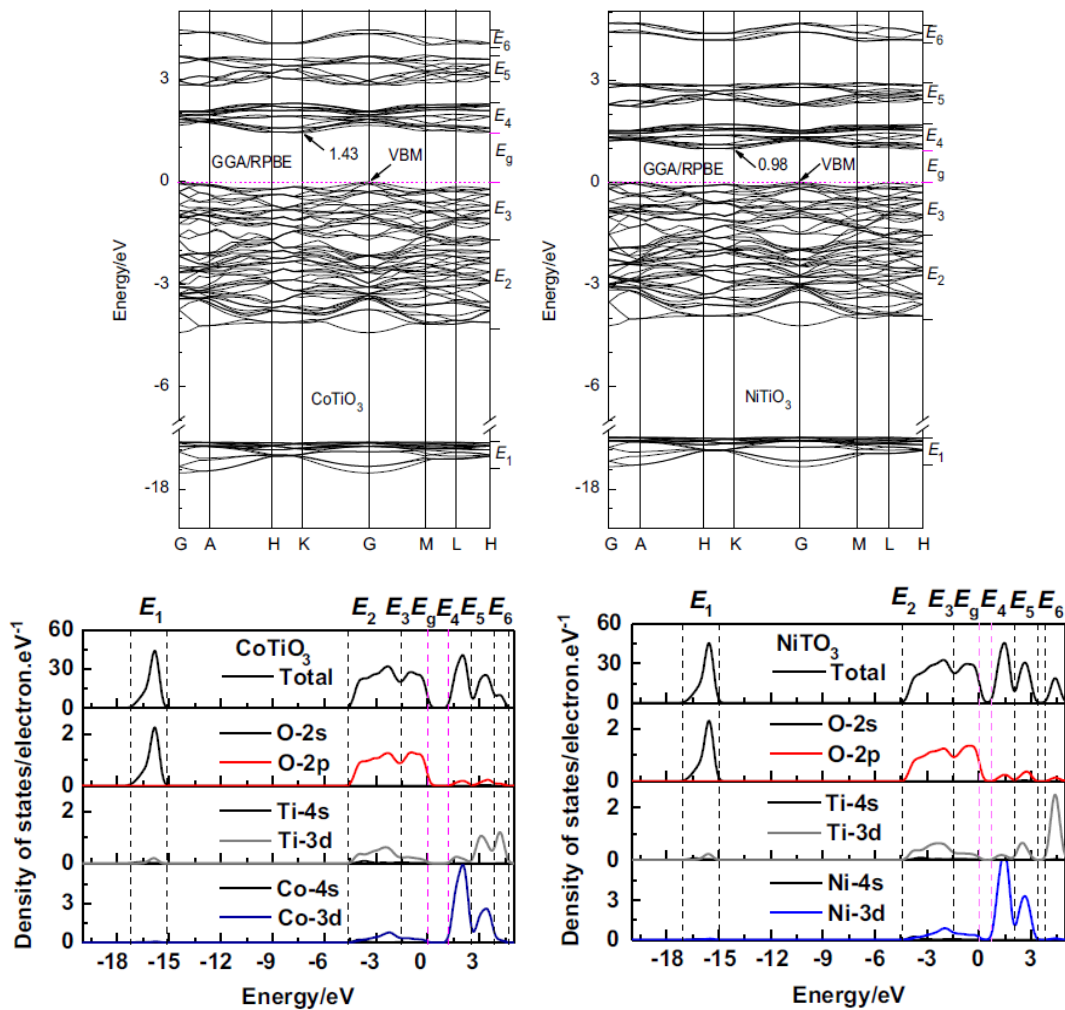
Figure 5. Band structures, total and partial density of states of (a) $CoTiO_3$, (b) $NiTiO_3$.

1.2 Carbon nitride materials

The first mention of polymeric derivative – melon – was made by Berzelius and Liebig in 1834. Melon is a linear polymer of interconnected tri-s-triazine through secondary nitrogen and it is considered one of the oldest artificial polymers reported in the scientific literature. The polymeric carbon nitride bulk (PCN bulk) became popular as a photocatalyst by Wang et al. in 2009, when it was the first time that a metal-free semiconductor material reported for the H_2 production. [34] This discovery, shifted the interest of research community in searching polymeric conjugated semiconductor photocatalysts, rather than inorganic materials. The widely used term in literature graphitic carbon nitride "g-C_3N_4" can not represent the real structure of C_3N_4 and is wrong because it is nonstoichiometric and studies of the structure by Lotsch et al. [35] in 2007, exhibited that the planar cohesion of the so-called g-C_3N_4 is mainly hydrogen bonding with NH/NH_2 groups, which is different from the planar covalent bonding cohesion of the graphite. However, in literature, it is still referred as g-C_3N_4 for historical reasons.

1.2.1. Structure of polymeric carbon nitride bulk (PCN bulk)

3D Carbon nitride have strong covalent bonds between sp^2-hybridized Carbon atoms and Nitrogen atoms in each layer, establishing the π-conjugated electronic structures and the layers each other are connected with weak Van den Waals interactions [36] with a layer distance of about 3.3 nm. [37] C_3N_4 can exist in seven phases, which are α-C_3N_4, β-C_3N_4, cubic-C_3N_4, pseudo-C_3N_4, g-h-triazine, g-o-triazine, g-h-heptazine. The basic units of the structure of carbon nitride involve triazine (C_3N_4) and tri-s-triazine/heptazine (C_6N_7) rings, are depicted in Figure 6A. Triazine is an aromatic compound with alternating arrangement of carbon and nitrogen atoms in the ring. Among all seven allotropes, tri-s-triazine is the most stable phase of C_3N_4 at ambient conditions and is regarded as the building block for the formation of polymeric carbon nitride. [38] There are different precursor materials used for the production of polymeric carbon nitride bulk at different annealing temperatures (Figure 6B). They include urea, thiourea, dicyandiamide, cyanamide and melamine.
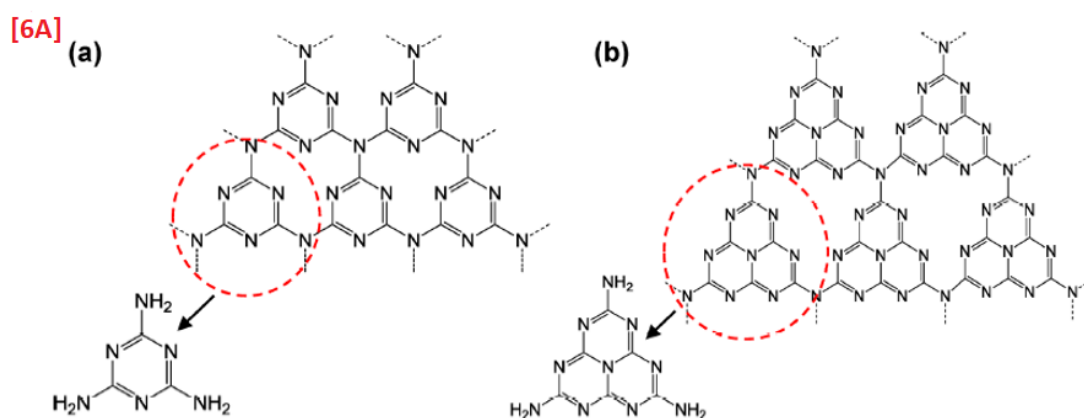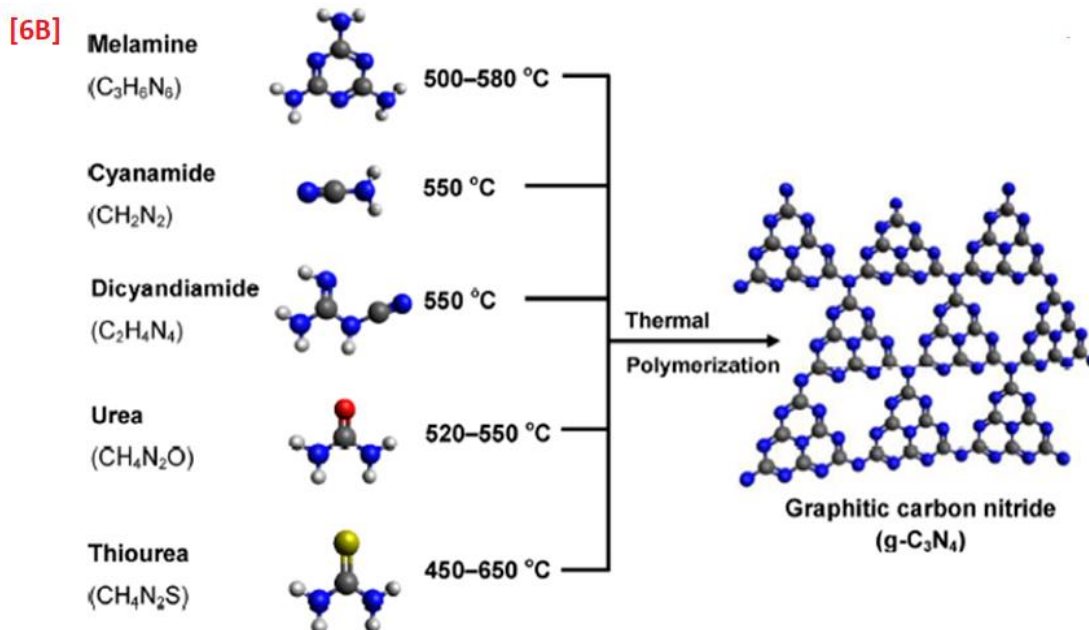
Figure 6. *(6A) The building blocks of polymeric carbon nitride; (a) 1,3,5-Triazine (C₃N₃) and (b) tri-s-triazine/heptazine (C₆N₇) and (6B) The pathway for the creation of polymeric carbon nitride bulk from different precursors.*

The most common pathway for the production of polymeric carbon nitride derives from the thermal condensation of cyanamide to dicyanamide and then to melamine. The second step is a condensation process in which ammonia is eliminated. At 350 °C melamine-products are present and at 390 °C the tri-s-triazine products are obtained from rearrangements of melamine. The final polymeric carbon nitride bulk is obtained at 520 °C, the increment of temperature above 600 °C makes the material unstable and by further heating above 700 °C, there is the generation of nitrogen and cyano fragments, the decomposition and finally the disappearance of the material.
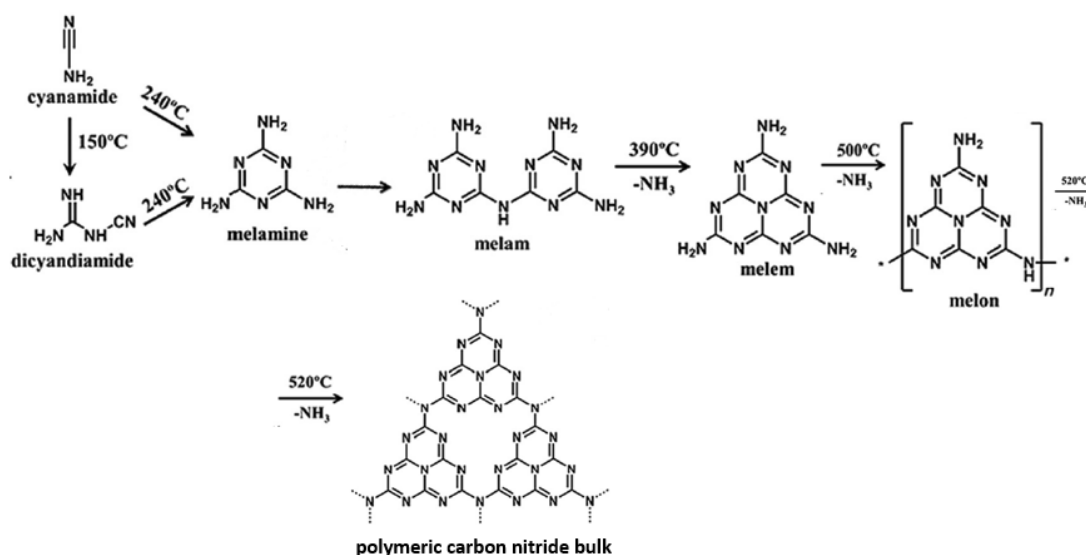
Figure 7. *The pathway for the creation of polymeric carbon nitride bulk.*

1.2.2 Preparation methods of Carbon Nitride nanosheets (CNNs)

2D nanostructures have been studied due to their unique physical and electronic properties. The structural two-dimensional anisotropy in nanoscale thickness compared to their microscale lateral size leads to new physicochemical properties due to the quantum confinement effect and opens new possibilities for applications. Inspiring by the widely used Hummers method [39], combining to the exfoliation of graphite to a monolayer or a few layers of graphene driving to the exceptional electronic, optical, mechanical and thermal properties of graphene rather than graphite, the research community wanted to isolate atomic-thick CNNs from polymeric carbon nitride (PCN) bulk. Therefore, the utilization of the available synthetic routes from graphite to graphene proved helpful for the development of these novel layered materials. Many preparation techniques were proposed for the creation of 2D covalent organic frameworks (COFs) of metal – free polymeric nanosheets, which can be categorized in two main strategies; the top-down approach and bottom-up approach, depicted in Figure 8. [40]
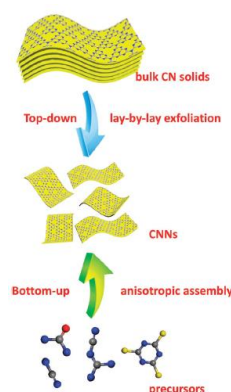
Figure 8. Strategies for the production of Carbon Nitride nanosheets (CNNs).

1.2.2.1 Top – down approach

Top-down approach includes the delamination of layered PCN bulk solids into nanosheets. The delamination can be accomplished with three main synthetic approaches. These include the post-thermal oxidation etching process, the ultrasonication-assisted liquid exfoliation route and the combination of thermal oxidation and liquid exfoliation.

1.2.2.1.1 Post thermal oxidation etching

Niu et al. in 2012, [41] by wanting to learn whether the hydrogen bonding is strong enough against oxidation effect exerted by $KMnO_4$ oxidant or not, tried to exploit the Hummers method in order to obtain CNNs from PCN. They found out that with Hummers method, the obtained material was particle-like of several hundred nanometers thick instead of nanosheets and that the planar atomic structure was destroyed. Therefore, they noted that the existence of a medium strong planar hydrogen bonding hampers the effectiveness of Hummers' method to produce CNNs. Therefore, they developed the direct thermal oxidation etching process of PCN in air, in which the hydrogen bond are not stable against oxidation process in air, will be oxidized from the bulk material and the thickness of bulk material will be decreased. The initial bulk

material consists of solid agglomerates with a size of several micrometers and annealing creates a layer-by-layer thermal etching process (see Figure 9). The resultant CNNs with a thickness of 2 nm and a size of ten micrometers, formed by 6-7 layers can be obtained by heating at 500 °C for 2 h in air.
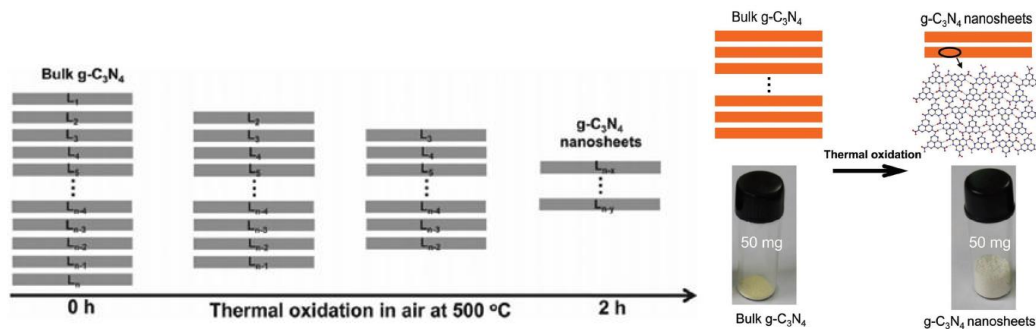
Figure 9. The exfoliation of carbon nitride bulk to nanosheets relating to annealing temperature.[41]

1.2.2.1.2 Ultrasonication-assisted liquid exfoliation

The ultrasonication-assisted liquid exfoliation technique demonstrated by Zhang et al. in 2012. They demonstrated the delamination of ultra-thin CNNs by a liquid exfoliation route in water via continuous ultrasonication. The obtained solution was stable under acidic and alkaline conditions. After this work, many research groups tried to delaminate PCN by this method with a change in solvents. [42] Another significant step in this procedure was made by Xu et al. in 2013 [43] and Ma et al. in 2014. [44] They tried to protonate carbon nitride by mineral acids, such as H_2SO_4 and HCl, because nitrogen atoms of carbon nitride can act as acceptor sites to facilitate the intercalation of acids.
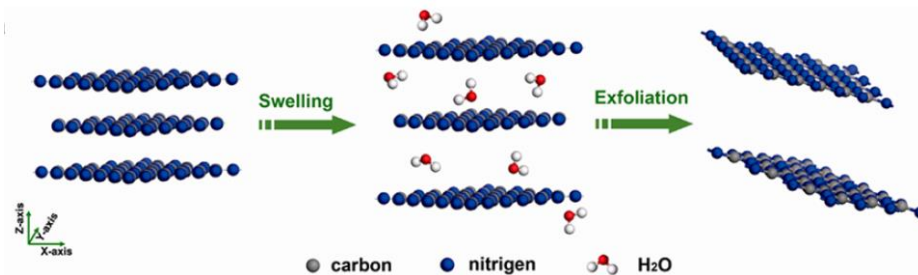
Figure 10. Liquid exfoliation process from carbon nitride bulk to ultrathin nanosheets.

1.2.3 Applications

Potential applications of polymeric carbon nitride bulk have been reported regarding the energy storage, solar cells, gas and humidity sensors. [45] However, PCN bulk deals with major drawbacks regarding its photocatalytic activity. These are its poor dispersion and solubility in water and the rapid rate of electron – hole recombination leading to limited photocatalytic efficiency. [46] Carbon nitride sheets exhibit distinct advantages compared to carbon nitride bulk. They possess a high specific surface area with abundant reactive sites associated with their opened-up flat structure; a property that is useful for light harvesting and mass transport. Their larger bandgap compared to

PCN bulk, due to the quantum confinement effect could contribute to higher percentage of visible light harvesting and stronger redox ability of charge carriers. The anisotropic structure along in-plane direction with a reduced thickness compared to PCN bulk reduces the perpendicular migration distance of charge-carriers from the bulk to the surface or in other words, the short bulk diffusion length and thus the recombination probability of photo excited charge carriers shortens. [40] Therefore, the facile preparation of CNNs, the suitable electronic band structure and the high physicochemical stability make it a promising material for heterogeneous photocatalysis. It literature, the reported applications include the usage of CNNs in photocatalytic activities such as at CO_2 reduction, organic waste degradation and photocatalytic water splitting for H_2 or O_2 production. [38]

1.3 Photocatalytic water splitting towards H_2 production

1.3.1 The energy problem

Industrialization and rapid growth of population have emerged the problem regarding the unlimited usage of fossil fuels. The world's energy demand is largely dependent on fossil fuels, such as coal, petroleum and natural gas. In addition to energy production, these sources are exploited thoroughly by industry for the manufacturing of plastics. Therefore, their consumption not only has a negative impact on the environment but also will inevitably lead to their depletion. This situation has made scientists searching how to exploit effectively the alternative sources of energy, such as solar energy. Among various researched methods, photocatalytic water splitting is a promising and green sustainable avenue that converts the inexhaustible solar energy to fuels (such as H_2). Hydrogen (H_2) has been recognized as a potential clean energy source, able to solve future energy limitations arisen from the depletion of fossil fuels.

1.3.2 Fundamental Principles

1.3.2.1 Electronic properties of semiconductors

The electronic structure of a semiconductor plays a key role to its properties as a photocatalyst. According to the band theory, when N atoms are connected, their atomic orbitals overlap and form bonding and anti-bonding molecular orbitals. As it is depicted in Figure 11, the bonding orbitals have lower energy than the single atomic orbitals that combined and the anti-bonding orbitals have higher energy than the atomic one. As the number N of the atomic orbitals increases, the number of molecular orbitals increases, too and the energy levels become denser. For a large number of atomic orbitals in a macroscopic solid, there is the creation of the valence and conduction band, which are the formed energy bands. The energy distance between them is a forbidden region, the energy gap (E_g) of the semiconductor. The valence band is the highest occupied band with electrons and the conduction is empty at ground state conditions. These bands are filled with the Pauli Exclusion Principle. [47],[48]
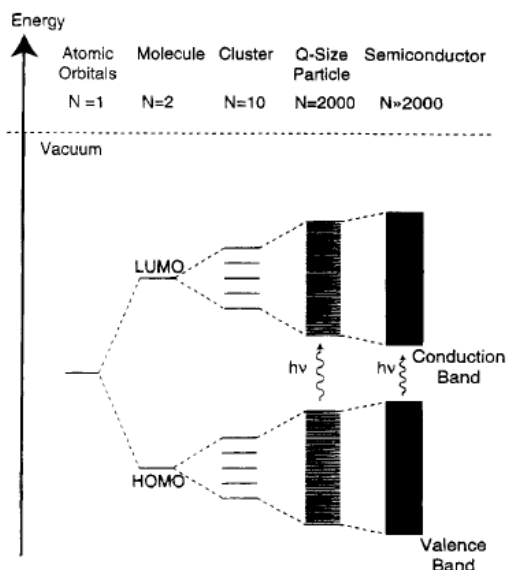
Figure 11. *The electronic structure from a distinct atomic orbital to a semiconductor.* [47]

This difference of the bandagap between the energy bands determines the electronic characteristics of a material and results in conductors, semiconductors and insulators (see Figure 12). A basic parameter to distinguish these three categories is the position of the Fermi level (E_F). The Fermi level represents the average work to remove an electron from a material (work function). If the Fermi level lies within a band and there is no difference in energy between the valence and the conduction band, then the material is a conductor. A semiconductor has a nearly filled valence band and a nearly empty conduction band and the energy that separates these two bands, is denoted as the energy gap of a material. The Fermi level in a semiconductor and an insulator lies in their bandgap. An insulator is a material with a large bandgap ($E_g > 4$ eV), which separates a completely filled valence band with an empty conduction band.
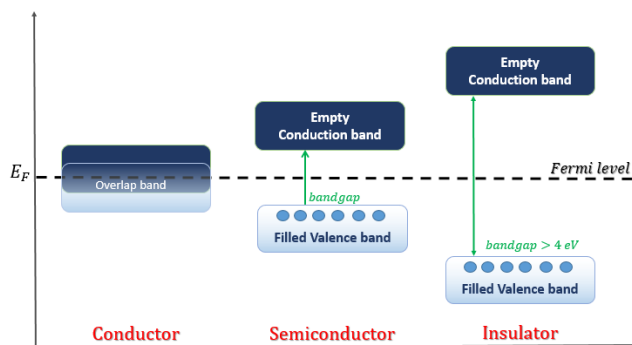
Figure 12. *Energy band diagrams for different types of materials.*

When a semiconductor comes in close contact with another phase, such as water, electrolyte or another semiconductor, an interface is created between them. Depending on the interface, a semiconductor is able to develop a built-in electric field which can facilitate the separation of charge carries and their transfer in one direction. In order to be formed the junction between the semiconductor and the second phase, the Fermi level (E_F) plays the key role in this procedure. When the two different phases come in contact, the electrons will flow from the phase of more negative E_F to the other phase,

in order to obtain the equilibrium. This process, where the bands bend to equilibrate the corresponding Ef is known as band-alignment. Therefore, the conduction band of the n-type semiconductor will be bent upwards and in that region, a space charge layer (SCL) is formed which contributes as an internal electric field. In Figure 13a, an n-type semiconductor and an electrolyte before come in close contact are depicted. While in Figure 13b, the band bending that created when these two phases came in close contact is illustrated. The IE corresponds to the ionization energy, ϕ is the work function and χ is the electron affinity. Ionization energy in the energy potential difference between the E_{vacuum} and the energy of the valence band edge. Electron affinity (χ) is the energy difference between the E_{vaccum} and the energy of the conduction band edge. The work function is the energy difference between the E_{vacuum} and Fermi level E_F. [49]
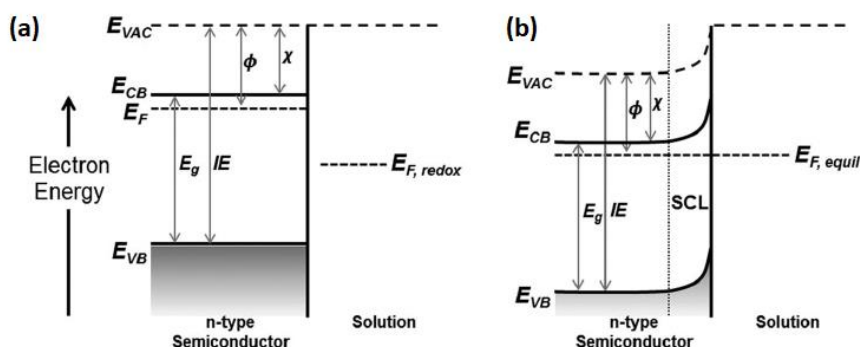
Figure 13. *The energy levels of semiconductor/electrolyte interface.* [49]

The interface is a significant term for heterogeneous photocatalytic processes, because in these systems the photocatalyst come in close contact with water and sacrificials in order to start the redox reactions.

1.3.2.2 Basic mechanism of heterogeneous photocatalysis

The landmark study regarding photocatalytic water splitting was published in 1972 by Fujishima and Honda. They created a Photoelectrochemical cell which contained a semiconducting electrode of TiO_2 and when they irradiated the electrode, they observed that oxygen evolution occurred at the TiO_2 surface and concomitant reduction led to hydrogen evolution at the platinum black electrode, both confirmed by analytical measurements. [50]
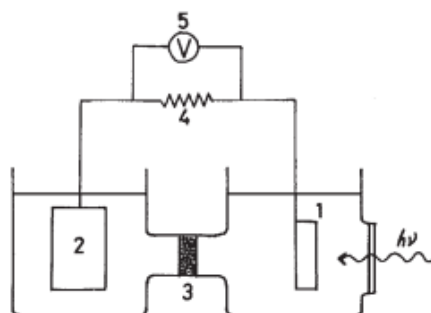
Figure 14. *Schematic representation of the Photoelectrochemical cell constructed by Fujishima and Honda in 1972.* [50]

Since this first observation, the semiconductor-based water splitting has been considered one of the most important approaches that could solve the world energy crisis, by focusing on the Hydrogen production as a combustible fuel, from water through energy conversion. Later, in 1982 Allen J. Bard was the first that designed a photocatalytic system, by using semiconductor particles or powders as photocatalysts instead of photoelectrodes. [51] The basic principle of photocatalytic water splitting is based on photosynthesis and starts with the irradiation of a photocatalyst with UV and/or visible light. A photocatalyst is a solid semiconducting material able to accelerate the photochemical reactions when it is irradiated with an appropriate amount of light. Therefore, if the given energy in the photocatalytic system is equal or higher than the energy gap of the semiconductor, the electrons are excited from the valence band to the conduction band, leaving positively charged holes in the valence band. After photo-excitation, the electrons and holes either recombine or migrate separated to the semiconductor's surface. This excitation creates a potential difference between the bands, which causes a reduction and an oxidation reaction to occur in conduction band and valence band, respectively. In valence band, the holes will oxidize the water molecules to form O_2, and in conduction band, the electrons will reduce the protons to form H_2. The photochemical redox reactions in a photocatalytic system are represented in the following equations. Eq. 6 describes the excitation of any semiconductor by light. Eq. 7 and 8 describe the reactions occur at the valence band and conduction band, respectively. [50]

$$semiconductor + 2hv \rightarrow 2e^- + 2h^+ \text{ (eq. 6)}$$
$$2h^+ + H_2O \rightarrow \frac{1}{2}O_2 + 2H^+ \text{(eq. 7)}$$
$$2e^- + 2H^+ \rightarrow H_2 \text{(eq. 8)}$$
$$H_2O \ (\ell) + 2hv \rightarrow \frac{1}{2}O_2(g) + H_2(g); \ \Delta G = +237 \ kJ/mol \ \text{ (eq. 9)}$$
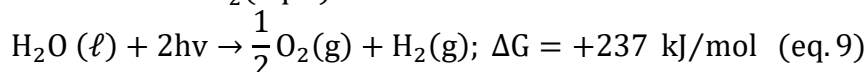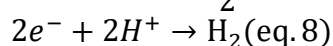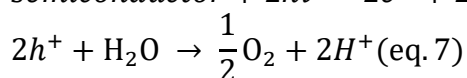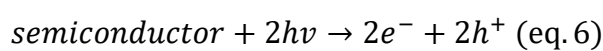
Water splitting into H_2 and O_2 is an uphill reaction[1]. It needs the standard Gibbs free energy change ΔG^0 of 237.2 kJ/mol or 1.23 eV, as depicted in eq. 9. The energy of 237.2 kJ/mol corresponds to the free energy change for the conversion of one molecule of H_2O to H_2 and half O_2 under standard conditions. The energy value of 1.23 eV corresponds to the water electrolysis potential according to the Nernst equation.

Since this landmark discovery, a lot of effort has been made in seeking photocatalysts with high activities. Metal oxides as photocalysts have a basic disadvantage; they are photoactive only in UV region, due to their wide bandgap. As it is depicted in Figure 14B, a small fraction of 5% of the incoming solar energy corresponds to UV light, rather than 43% that belongs to visible light. Therefore, the bandgap of an ideal photocatalyst should have energy gap $E_g \geq 1.23$ eV ($\lambda \leq 1000$ nm) but also $E_g < 3.0$ eV in order to absorb as much visible light as possible.

---

[1] **uphill reactions**: not spontaneous, results in increase in free energy (more energy in products than in reactants). required energy.
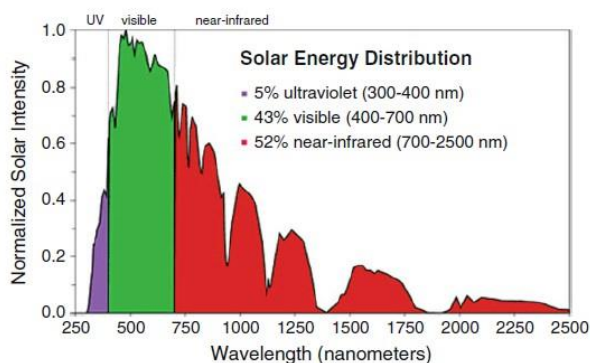
Figure 14B. *The solar energy distribution.*

Except from the energy band gap value of the semiconductor, another crucial requirement for water splitting involves the suitable band levels of the semiconductor, namely the potential values of the conduction and valence band. The bottom level of the conduction band has to be more negative than the reduction potential of H^+/H_2 [0 V vs normal hydrogen electrode (NHE)], whereas the top level of the valence band has to be more positive than the oxidation potential of O_2/H_2O (1.23 V). In Figure 15-left, an ideal photocatalyst with suitable flat band edges for H_2 and O_2 production through photocatalytic water splitting is depicted. In addition, as it seems in Figure 15-right the photocatalyst should be able to generate excited charges rather than generate phonons or heat, to separate and to transport fast the charges. [52] It is commonly called as the efficiency of the photocatalyst, namely its ability to generate the absorbed photons in excited charges; high efficiency is related to the conversion of a great amount of absorbed photons in excited charges. Generally, the produced H_2 is linked to the amount of excited e^-, that finally managed to be transferred in the water/photocatalyst interface, not to recombine in reducing water and are capable of initiating redox reactions.
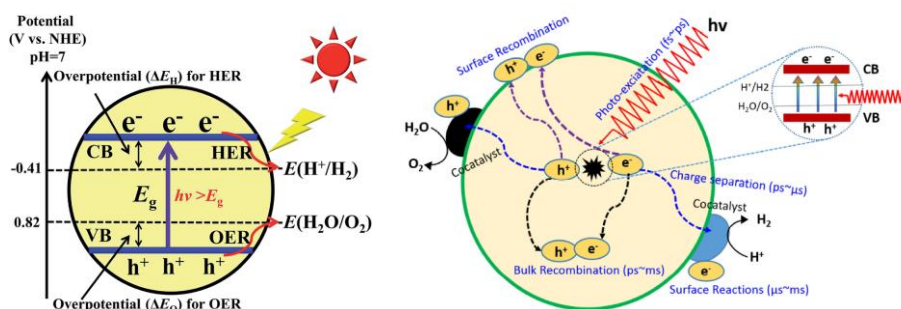
Figure 15. Left; *an ideal photocatalyst for water splitting and* ***Right;*** *Processes taking place in an illuminated photocalyst.*

Reflection and scattering of light should also be minimized in photocatalytic process. A deactivation process is ineffective for the photocatalyst and is related to the charge recombination, which can take place either at photo catalyst's surface or in bulk. Charge recombination reduces the excited charges by emitting light or generating phonons[*4]. The separation of excited electrons and holes needs to overcome an energy barrier which is the binding energy of the excitons[2]. The last requirement for a suitable photocatalyst is to remain stable, to have corrosion resistance in aqueous solutions and

---

[2] exciton | is a bound state of electron and hole pairs, attracted each other by electrostatic Coulomb forces.

not to suffer from oxidation. To test the photocatalytic stability a number of sequential experiments is required in order to be tested the photocatalytic activity of the catalyst, after several cycles or a long-termed experiment is required. [53]

1.3.2.3 The role of sacrificial reagents

Another process that is undesired in photocatalytic activities is the reaction of generated H_2 and O_2 onto the photocatalyst's surface to form H_2O, which is called "Surface-back reaction". One strategy to suppress this reaction involves the addition of sacrificial reagents into the photocatalytic system, which are consumed during the redox reactions, suppress the backward reaction and isolate either H_2 or O_2 as the final product. The sacrificial reagents are either electron donors or electron acceptors that are added in the system in order to work as an external driving force for the surface chemical reaction and depress the H_2O formation from H_2 and O_2. More specifically, when in the photocatalytic system exists an electron donor, an energy state trap is inserted above the top of the valence band and the photogenerated holes are transferred to this energy state trap (Figure 16). There, the holes will react with the electron donors and will oxidize them, instead of water. Therefore, the photogenerated electrons in the conduction band are able to reduce water and form H_2.
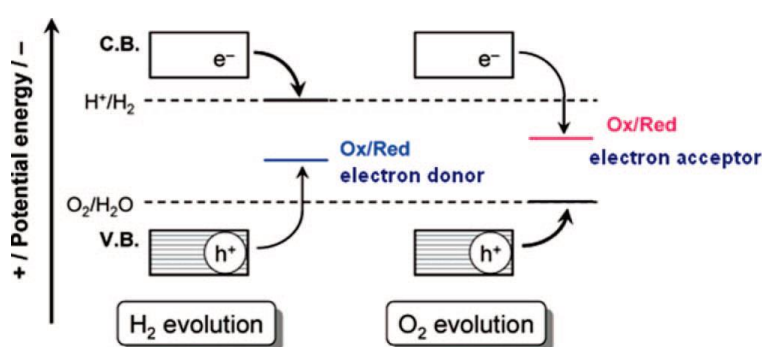
Figure 16. *Processes taking place in an illuminated photocalyst when sacrificial reagents are used.*

In general, in photocatalytic experiments, there have been used inorganic or organic sacrificial reagents. The organic compounds used as electron donors for photocatalytic hydrogen generation include alcohols such as methanol, ethanol, isopropanol etc., organic acids; such as formic acid, acetic acid etc. and aldehydes such as formaldehyde, acetaldehyde etc. The process for H_2 production with methanol as sacrificial reagent is described as follows. In eq. 10 is depicted the product formaldehyde (HCHO) that is further oxidized to methanoic acid (HCOOH) and subsequently to CO_2 together with H_2 generation. [53]

$$h^+ + H_2O \rightarrow \cdot OH + H^+ (eq. 10)$$
$$CH_3OH + \cdot OH \rightarrow \cdot CH_2OH + H_2O \ (eq. 11)$$
$$\cdot CH_2OH \rightarrow HCHO + H^+ + e^- \ (eq. 12)$$
$$2H_2O + 2e^- \rightarrow H_2 + 2OH^- (eq. 13)$$
$$overall \ reaction: CH_3OH \xrightarrow{hv,catalyst} HCHO + H_2 \ (eq. 14)$$

$$HCHO + \text{H}_2O \xrightarrow{hv,catalyst} HCOOH + \text{H}_2 \text{ (eq. 15)}$$

$$HCOOH \xrightarrow{hv,catalyst} CO_2 + \text{H}_2 \text{ (eq. 16)}$$
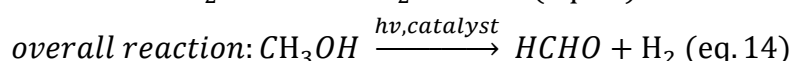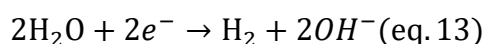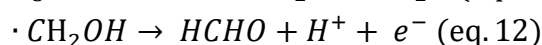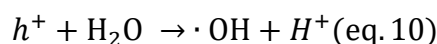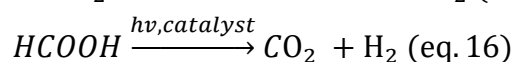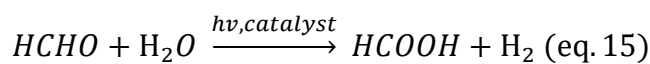
1.3.2.4 Approaches to modifying the electronic band structure for visible-light harvesting

Up until today, it has not been developed a single semiconductor that can utilize the solar light, possesses appropriate band edges to drive the redox reactions and exhibit stability in electrolytes. Therefore, to develop more efficient visible light driven photocatalysts, it is important to modify the bandgap of UV-active materials, by narrowing it. These modifications include element doping, catalyst loading, heterojunction formation with other materials and surface modification. The purpose of modification techniques is to tune the semiconductor's bandgap and band edges. [54]

1.3.2.4.1 Effect of Catalyst loading

By loading other materials (noble metals or metal oxides) – cocatalysts onto the photocatalyst, its structure does not change, as it happens in the element-doping category. The loading happens onto photo catalyst's surface to trap photo-excited electrons, via the differences in the Fermi level of each material, by making a heterojunction in order to produce active sites. It is a way to prevent electron recombination and enhance the charge separation. In not effective photocatalysts, the electrons tend to recombine due to low electron mobility by defects (defects usually act as recombination centers for photo-excited electrons and holes). The amount of loading catalyst is quite important, though; an excessive amount will cover the surface of the photocatalyst and will prevent light from reaching it. However, a low amount of loading catalyst can be dispersed uniformly resulting in low separation of electrons and holes. The catalysts can react as ultramicro-closed circuit photoelectrochemical cells to increase the H_2 evolution rate. [54]

1.4 Metal titanates as potential water splitting photocatalysts

Metal titanates are photoactive materials but exhibit low photocatalytic performances due to their wide bandgap or unsuitable band alignment relative to the water redox potentials. Specifically, $NiTiO_3$ and $CoTiO_3$ correspond to the visible range of the solar spectrum, but their lowest conduction band is located at a more positive potential than the reduction potential for H^+ to H_2. In Figure 17, all the metal titanates are represented with $SrTiO_3$, $CaTiO_3$, $MgTiO_3$ and $ZnTiO_3$ to have the appropriate conduction band edge for the water reduction towards H_2 production, but their wide bandgaps limit their absorption of the solar spectrum to only UV light. As already mentioned, UV-light responds to 5% of the total illumination inserting in earth, so, semiconductors' wide bandgaps result in low efficiency – because of the recombination of electron-hole pairs and the small fraction of UV region – and render them unsuitable for practical and industrial applications. [54]
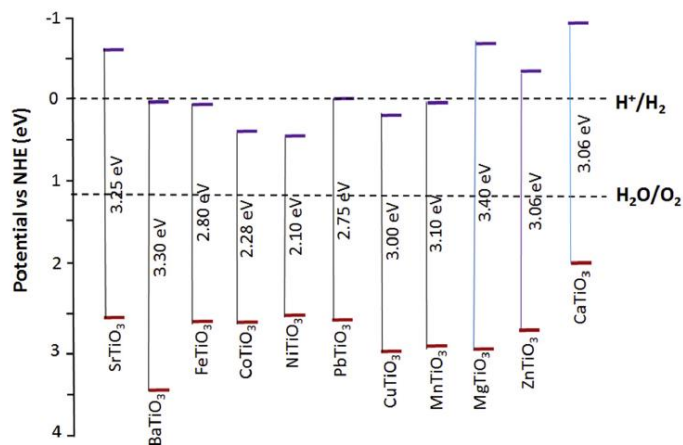
Figure 17. Metal titanates and their bandgaps and band edges with respect to the redox potential of water splitting. [54]

1.4.1 Heterostructures of metal titanates with carbon nitride nanosheets

As already mentioned, the unique properties of metal titanates have made them possible candidate photocatalysts for water splitting applications. Nevertheless, characteristics regarding their bandgap or their unsuitable band edges make them inactive, so the modification analyzed in Chapter 1.3.2.2; such as catalyst loading is a way to enhance photocatalytic activity of titanates for water splitting applications. The combination of metal titanates with CNNs seems promising because these individual materials exhibit interesting photocatalytic properties but these configurations suffer from certain drawbacks. These drawbacks include the unsuitable band edges, the wide bandgap of metal titanates and the high recombination rate of photo generated electron-hole pairs of CNNs. Therefore, the idea of creating a heterostructure between metal titanates and CNNs seems a promising way to get over these individual limitations. This heterostructure is considered favorable to separate the electron – hole pairs, offer higher charge mobility and low the recombination rates of charge carries. [3]

More specifically, as it has already been mentioned, $ZnTiO_3$ has gained the researchers' interest due to its outstanding properties and broad applications. However, its wide bandgap makes it able to be activated only in UV region, therefore its efficiency is low. However, its combination with another more suitable photocatalyst such as CNNs could probably enhance its photocatalytic activity in visible region and may enhance the separation of recombined electron and hole pairs. In literature, the heterostructure of $ZnTiO_3$ with CNNs was reported for photocatalytic H_2 production, by Pawar et al. in 2017. [55] They used a ratio of (40:60 w/w) $ZnTiO_3$:CNNs, with 1 wt% Pt as co-catalyst in a sacrificial agent of triethanolamine solution (10 vol%) under visible-light irradiation and the obtained photocatalytic activity was 50 μmol/g·h. Regarding nickel titanates combined with CNNs, reports in the literature include their use in photocatalysis for the degradation of Rhodamine B (RhB) [56] and methylene blue dye [57], [58] under visible light illumination. Up until today, the only mention for the creation of the heterostructure of $NiTiO_3$ with CNNs for photocatalytic H_2 production was made by Zeng et al. in 2016. [59] They created a heterojunction of PCN-3wt% $NiTiO_3$, with 1 wt% Pt as co-catalyst. The H_2 photocatalytic activity of this heterojunction was 835 μmol/g·h and is attributed to the high amount of CNNs. [59] In

literature, only two reports exist about the heterostructure of $CoTiO_3$ with CNNs. This heterostructure was used for the degradation of methyl orange [60] and for photocatalytic water splitting towards H_2 production under visible light illumination. More specifically, 0.15 wt% $CoTiO_3$-CN, with 3 wt% Pt as cocatalyst in ethanol as a sacrificial reagent and the H_2 production rate was 800 μmol/g·h. Finally, there are not reported studies for the heterostructure of $MgTiO_3$ with CNNs.

1.5 Master's thesis objective

The immense need for energy made scientists to seek for alternative, clean sources of energy, other than fossil fuels. Photocatalytic water splitting towards H_2 production is an ecofriendly method that aims to solve the energy problem, by converting water to hydrogen with the aid of a photocatalyst. Hydrogen is an essential fuel, necessary to be produced in a large scale in order to face the energy need. Up until now, the synthesized photocatalysts are not sufficient for industrial applications; therefore, the research community is focused on trying to develop an ideal photocatalyst. The objective of this Master thesis is the effort to exploit two different kinds of photocatalysts, each of them has its own special characteristics, and by combining them to create a novel, functional heterostructure able to split water towards H_2 under visible light irradiation. The dominant idea is to conjugate metal titanate rods with small exposed facets of CNNs. These exposed facets will act as sensitizers in order to enable and enhance the photocatalytic activity of metal titanates towards H_2 production. These facets will facilitate the charge transfer and the separation of photogenerated electrons – holes, due to the transfer of the charges across the formed interface of these two photocatalysts. Combining the unique properties of metal titanates with CNNs, which is a promising, metal free photocatalyst with advantageous properties regarding its photocatalytic activity, would be a promising avenue in order to discover a novel potential photocatalyst. In literature, there are no reports regarding the heterostructure with metal titanates to be the dominant photocatalyst and CNNs to possess only a small amount of the total material. In addition, all the reported works use Pt loading as a cocatalyst, which is unsuitable for scale-up applications. Therefore, our work differentiates from the above-mentioned reports, in the way that we tried to load a small amount of CNNs in order to activate metal titanates. In addition, in this work, we did not use complicated synthetic procedures or sample's loading with Pt in photocatalytic experiments. Finally, all the experiments carried out under UV-visible light illumination because we attempt to create a simple system in order to be utilized for scale-up applications.

Chapter 2 – Experimental Section

All of the chemicals used in this thesis for the synthetic procedures and for the photocatalytic experiments were analytical-grade and used without further purification. For the synthesis of metal titanates rods the precursors include magnesium acetate tetrahydrate Mg $(CH_3COO)_2 \cdot 4H_2O$ ($\geq$ 98.0%) and cobalt (II) acetate tetrahydrate $Co(CH_3COO)_2 \cdot 4H_2O$ ($\geq$ 98.0%) were purchased from Alfa Aesar. Ethylene glycol $HOCH_2CH_2OH$ (99.5%) was purchased from Honeywell and Sodium hydroxide pellets (99.0%) were purchased from Riedel-de-Haen. zinc acetate dihydrate Zn $(CH_3COO)_2 \cdot 2H_2O$ (99.99%), nickel (II) acetate tetrahydrate (99%), Ni $(CH_3COOH)_2 \cdot 4H_2O$, titanium (IV) butoxide $Ti(OCH_2CH_2CH_2CH_3)_4$ ($\geq$ 97.0%) were purchased from Sigma Aldrich. For the preparation of CNNs, melamine $C_3H_6N_6$ (99.0%) was purchased from Sigma Aldrich. For the above mentioned procedures ethanol (99.0%) by Honeywell, isopropyl alcohol (99.8%) by Fisher and nanopure water were used.

2.1 Synthesis of metal titanate rods $MTiO_3$ (with M=Mg, Ni, Co, Zn)

Metal titanate rods were prepared according to a modified sol gel, organic ligand coordination polymerization method at room temperature. [26] The synthetic procedure involves 5 mmol of metal acetates [1.07 g of $Mg_{(ac)}$, 1.24 g of $Ni_{(ac)}$, 1.24 g of $Co_{(ac)}$, 1.095 g of $Zn_{(ac)}$], dissolved in 30 ml of ethylene glycol (EG) under vigorous stirring. Then, 5 mmol (1.7 ml) of titanium butoxide were added dropwise and the suspension was left under continuous stirring for 10 min at room temperature (RT). Then, 5.5 mmol (0.22 g) of Sodium hydroxide pellets were added to the suspension and the suspension was left at continuous stirring for 24 h, at room temperature (RT). Then, the suspension was centrifuged for 30 min at 4,000 rpm and the precipitate was collected and purified two times with ethanol for 15 min at 4,000 rpm each. Then, the produced gel, dried in air at 200 ºC for 12 h with an increment rate of temperature of 20 ºC/h and left to cool down naturally to room temperature. The obtained powders were ground into an agate mortar and were then sintered in air at different temperatures (400 ºC, 600 ºC, 800 ºC) for 2 h with an increment rate of temperature at 5 ºC/min and left to cool down naturally to RT temperature. The above-mentioned synthetic procedure was followed for the formation of $MgTiO_3$, $NiTiO_3$, $CoTiO_3$ and $ZnTiO_3$ rods.

2.2 Preparation of Carbon nitride nanosheets (CNNs)

A two-step, modified process was followed for the preparation of carbon nitride nanosheets. [41] Firstly, 40 mmol (5 g) of melamine were annealed into a covered ceramic crucible combustion boat at 500 ºC for 2 h and 520 ºC for 2h in air, with an increment rate of temperature of 2 ºC/min and left to cool down naturally to room-temperature. The yellow obtained powder, denoted as carbon nitride bulk, was transferred in an opened-air ceramic crucible and annealed at 520 ºC for 2h in air, with an increment rate of temperature at 2 ºC/min and left to cool down naturally to room-temperature. The produced material is denoted as porous CNNs.

2.3 Combination of the heterojunction of metal titanates with CNNs

A designated amount of metal titanate rods and CNNs was dispersed in isopropyl alcohol in separated vials, transferred into a sonication bath and remained for 1 h. Then, the two different suspensions were mixed under continuous stirring overnight. The dried powder was annealed at 300 °C for 1 h with an increment rate of temperature of 5 °C/min and left to cool down naturally to room-temperature. Finally, the annealed powder was ground into an agate mortar.

2.4 Structural, morphological and optical properties

2.4.1 Powder X-Ray Diffraction (PXRD)

X-ray diffraction patterns of powders were obtained by a Bruker AXS D8 Advance copper anode diffractometer (CuKa radiation), equipped with a Nickel foil monochromator operated at 40 kV and 40 mA over the 2θ collection range of 10°-80°. The scan rate was 0.05 s⁻¹.

2.4.2 Scanning Electron Microscopy (SEM) and Energy Dispersive X-Ray Spectroscopy (EDS)

Surface morphology and elemental analysis of the samples were carried out using scanning electron microscopy (SEM), a JEOL JSM-6390LV instrument at an acceleration voltage of 20 keV and energy dispersive spectrometry (EDS).

2.4.3 Transmission Electron Microscopy (TEM)

The microscopic nanostructures were studied by transmission electron microscopy (TEM) operating at 200kV (JEM-2100 instrument equipped with LaB_6 filament).

2.4.4 Ultraviolet–visible spectroscopy (UV-Vis)

The UV – Visible diffuse reflection spectra of the powders were measured on a UV-2600 Shimadzu UV-Vis spectrophotometer, using $BaSO_4$ powder, as a 100% reference reflectance standard. Diffuse reflectance was converted into absorption over scattering using the Kubelka – Munk function, F(R).

$$K.M. function = \text{F(R)} = \frac{\text{k}}{\text{S}} = \frac{(1-\text{R})^2}{(2\text{R})} \ (eq.\ 17)$$

In eq.17, R is the measured Reflectance, k and S are the absorption and scattering coefficients, respectively. The standard equation for the estimation of the energy bandgap E_g is the following:

$$[\text{F(R)} \cdot \text{hv}]^{1/\text{n}} = A\ (E_g - hv)\ (eq.18)$$

In eq. 18, hv is the photon energy and **n** is related to the allowed and forbidden transitions in a semiconductor. For an indirect allowed transition n = 2 and for a direct allowed transition n = 1/2. Therefore, the energy bandgaps (E_g) were estimated by plotting the $[F(R)h\nu]^{1/n}$ vs photon energy, hv (eV).

## 2.5 Photocatalytic experiments towards H_2 evolution

The photocatalytic reduction of water towards Hydrogen evolution reaction (HER) activity was performed in a water-cooled pyrex reaction vessel, which irradiated at λ>360 nm light using a 300 W Xenon lamp. In the pyrex reactor the catalyst was suspended with vigorous stirring in 20% (v/v) aqueous methanol solution (20 ml). The suspension was first purged with Ar flow for at least 30 min to ensure complete removal of oxygen and then irradiated with UV/Vis light (λ > 360 nm). The produced H_2 gas was detected by taking 100 μL of gas using a gas tight syringe and was analyzed by GC (Shimadzu GC-2014 equipped with a TCD detector), using Ar as the carrier gas.

Chapter 3 – Results and Discussion

3.1 Synthesis, characterization, photocatalytic activity of metal titanates

3.1.1 Synthesis of metal titanates (where metal M=Mg, Ni, Co, Zn)

The synthesis of metal titanate rods was a modified, sol-gel based ethylene-glycol chemical process at room-temperature. [26] A schematic view of the synthetic procedure is depicted in Figure 18 for all the metal titanates, respectively.
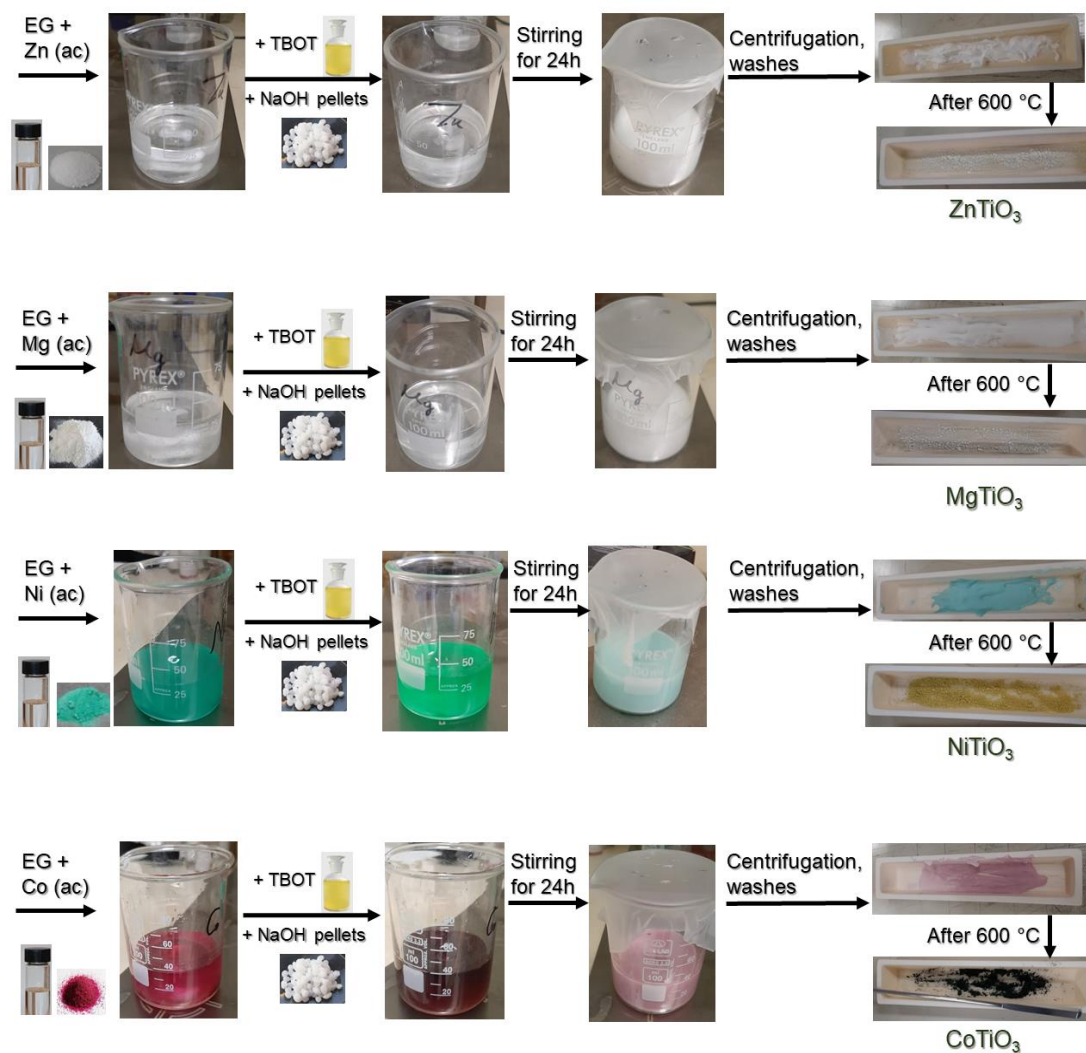
Figure 18. *The synthetic procedure of metal titanates.*

At first, metal acetate was added into ethylene glycol which was used as a solvent and complexing agent, by forming a suspension. Then, equal quantity in molar ratio of titanium butoxide compared to metal acetate was added into the suspension and the suspension became more homogeneous. The suspension was left for 10 minutes under vigorous stirring until the total dissolution of TBOT. The quantity of Titanium butoxide was selected as a 1:1 atomic ratio compared to metal acetates, in order to be obtained stoichiometric metal titanates. Sodium hydroxide pellets were added into the suspension. Finally, the suspension was left under vigorous stirring for 24 h. Then, the

suspension was centrifuged, the precipitate was collected and washed. The final product formed a gel which was dried at 200 ^{o}C for 12 h in an oven. After drying, the obtained powders were ground into an agate mortar and were then annealed in air at different temperatures for 2 h, in order to obtain metal titanate rods. The above-mentioned synthetic procedure was followed for the formation of $MgTiO_3$, $NiTiO_3$, $CoTiO_3$ and $ZnTiO_3$ rods.

The following optimization experiments were designed in order to determine the best synthetic parameters of the final synthetic procedure. These parameters involve the metal salt source, the acidic or basic environment of the reaction controlled by the pH and the enhanced humidity. Two types of metal salt sources were examined, including metal oxalate and metal acetate. The initial stoichiometry in this procedure of M:Ti:EG was 1:1:100 and chosen by literature [26]. SEM measurements are depicted in Figure A1-A2, in the Appendix section, where it is clear that this system is favored by the use of metal acetate in order to be obtained rod-like metal titanates, possibly because of the pH value of the reaction, that differs when these two salts are used in the reaction. Therefore, a second parameter that was examined was the acidic environment of the reaction that was succeeded with the use of acetic acid in the system of $M_{(ac)}$:Ti:EG in a molar ratio of 1:1:100 and SEM images revealed an amorphous material and EDS measurement revealed a molar ratio of Mg:Ti to be 2:98. In addition, in order to study the system in alkali pH, in the $M_{(ac)}$:Ti with a molar ratio of 1:1, EG and different quantities of NaOH were added. SEM images, revealed the rod-like shapes are favored in alkali pH.

The annealing at 600 ^{o}C found out to be the most favorable for the formation of metal titanate rods and was optimized through different low and high temperatures of annealing.

3.1.2 Morphological, structural and optical properties

PXRD, SEM and TEM techniques were used in order to examine the structural and morphologicals characteristics of the particles into the powder. EDS measurements were carried out at the samples before the annealing process in order to examine the stoichiometry of the metals in the metal complex. Then, when the stoichiometry of the metals M:Ti was 1:1, the annealing of the powders was followed at temperatures 400 ^{o}C, 500 ^{o}C, 600 ^{o}C and 800 ^{o}C. These three temperatures were selected in order to examine the formation of metal titanates in low, intermediate and high temperatures. Optical measurements in a range from ultraviolet to infra-red (200-1,400 nm) were conducted in order to exclude meaningful information about the potential photocatalysts, regarding their spectrum of absorption and their energy band gaps. The measured reflectance of the powders was converted into absorption/scattering, using the Kubelka-Munk function as it was analyzed in section 2.4 and then the energy gaps of the powders were estimated.

### 3.1.2.1 Cobalt Titanate (CoTiO$_3$) rods
The EDS measurement for the powder before the annealing process revealed a molar ratio of 1:1 between the two metals of Co and Ti (see Figure A3 in the Appendix section). Therefore, the annealing of the powders was followed at temperatures 400 ^{o}C,

600 °C and 800 °C and the PXRD graphs are depicted in Figure 19. The molar ratio at different annealing temperatures is depicted in Table 1, where at all different temperatures of annealing, the molar ratio of cobalt and titanium is equal.

**Table 1.** *The molar ratio between cobalt and titanium at all different temperatures.*

Annealing temperature	Atomic % (Co:Ti)
Before annealing	1:1
400 °C	1:1
500 °C	1:1
600 °C	1:1
800 °C	1:1

The PXRD graph for the powder before annealing reveals its amorphous phase, which has not been formed before the annealing process. The annealing at 400 °C and 500 °C reveals that the material is still amorphous and has not been crystallized, yet. At 600 °C, the phase of $CoTiO_3$ is clear, with a high degree of crystallinity, revealed from the strong and narrow peaks. At an even higher temperature of 800 °C, the phase of $CoTiO_3$ remains unchanged, without the formation of any other second phase or impurities. Therefore, the optimal annealing temperature for the formation of $CoTiO_3$ was 600 °C, as an intermediate temperature compared to 800 °C.
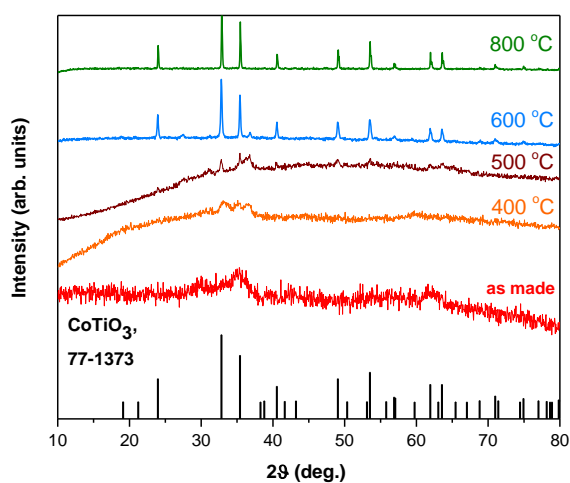
Figure 19. *X-ray diffraction pattern for $CoTiO_3$ for all different annealing temperatures.*

The characteristic X-ray diffraction peaks revealed at 600 °C (see Figure 20) at $2\vartheta = 23.80°, 32.80°, 35.25°, 40.35°, 48.90°, 53.35°, 56.85°, 61.85°, 63.60°, 70.85°, 74.75°$ are attributed to $(012), (104), (110), (11\bar{3}), (024), (11\bar{6}), (018), (12\bar{4}), (300), (1010), (220)$ reflections for ilmenite $CoTiO_3$ (JCPDS card number no. 77-1373). $CoTiO_3$ belongs to the Rhombohedral crystal system, at space group $R\bar{3}$ with space group number 148. No characteristics peaks of other impurities such as TiO_2, CoO, Co_2O_3, Co_3O_4 are observed. The strong and narrow diffraction peaks reveal the high crystallinity of the synthesized material.

25
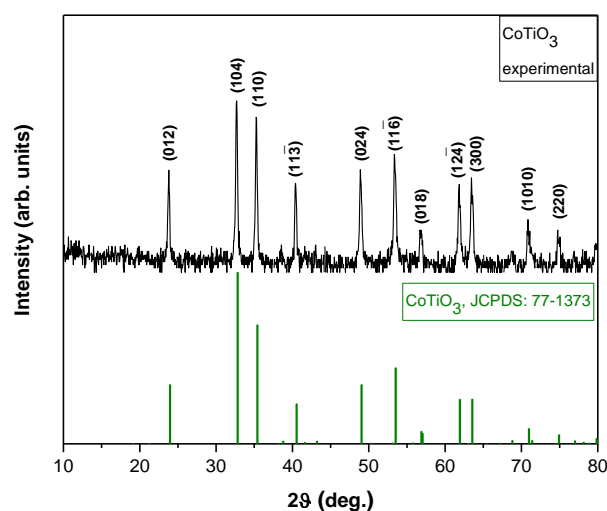
Figure 20. X-ray diffraction pattern of CoTiO₃ annealed at 600 ᵒC.

The experimental lattice parameters for cobalt titanate at 600 °C were estimated and are depicted in Table 2. The experimental cell parameters are close to the theoretical values.

Table 2. Lattice parameters of CoTiO₃

CoTiO3	Cell parameters			Angles (degrees)			Volume
	a (Å)	b (Å)	c (Å)	a	β	γ	Å³
theoretical	5.0662	5.0662	13.9180	90	90	120	309.37
experimental	5.0620	5.0620	13.9131	90	90	120	308.7

Regarding the morphology of the sample, the rod-like conformation of CoTiO₃ powder was revealed by SEM observations, before and after the different annealing temperatures. In Figure 21, SEM images are illustrated, where the length of the hexagonal rods is about 1-2 μm and their diameter is about 200 nm. Compared with the precursor, the length and diameter of the rods remain the same after the different annealing temperatures. It is also depicted that at 800 °C, the particles of CoTiO₃ have formed agglomerates around the rods and there is no homogeneity.
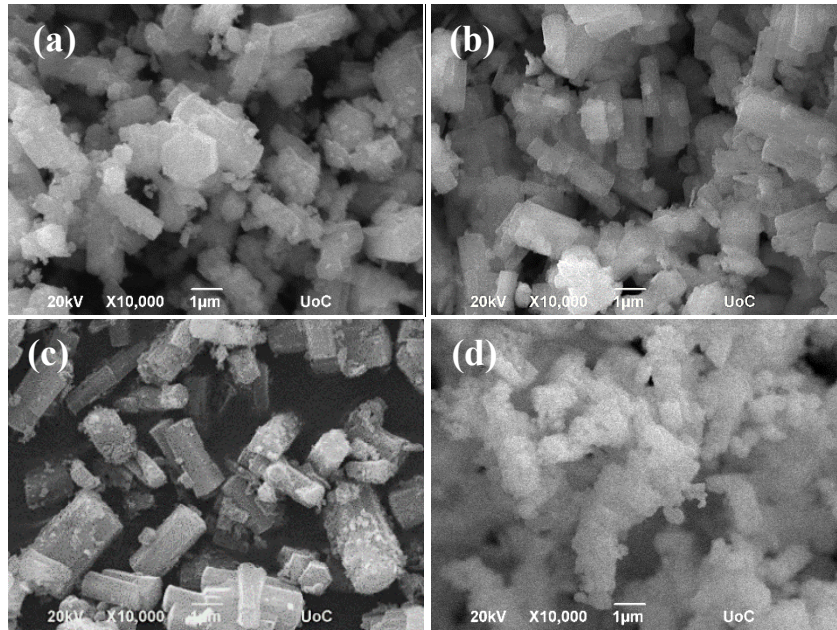
Figure 21. SEM images of cobalt titanate rods (a) before annealing and at different annealing temperatures (b) 400 ºC (c) 600 ºC (d) 800 ºC.

The homogeneity of all the individual elements in the rods annealed at 600 ºC is presented by the EDS mapping technique, where the colored dots represent each element.
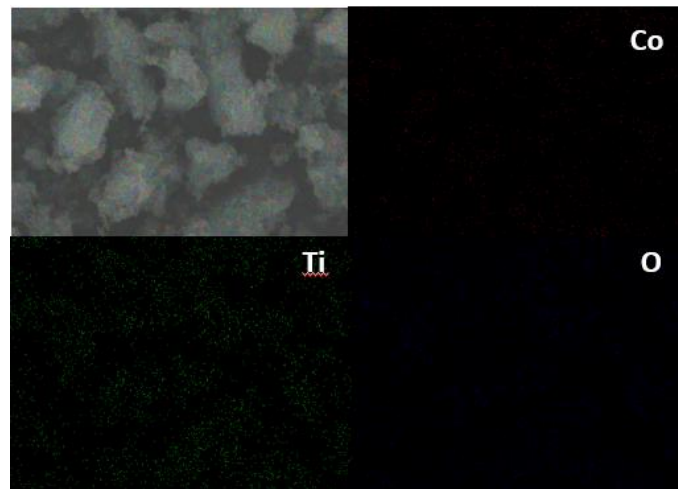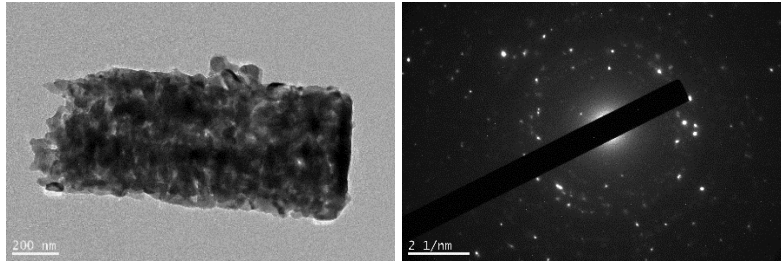

Figure 22. EDS mapping images of Cobalt titanate rods.

In order to receive more information about the morphology of $CoTiO_3$, TEM was used. In Figure 23, TEM pictures present the rods, with length l=1μm and diameter d=200-500 nm and reveal that cobalt titanate rods are composed by nanoparticles and pores. The SAED pattern reveals the polycrystallinity of the sample.
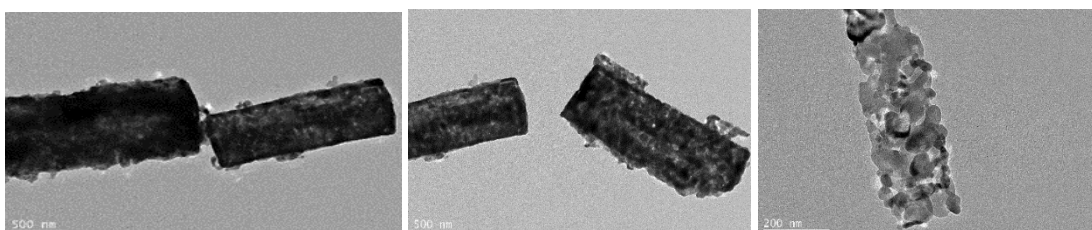
Figure 23. TEM pictures and SAED pattern of CoTiO₃

CoTiO₃ demonstrates a photo absorption in both UV and visible region of the spectrum (see Figure 24). In visible region, a broad absorption edge at 540 nm is associated with the optical band gap attributed to the $O^{2-} \rightarrow Ti^{4+}$ charge transfer interaction. In the visible region, two absorption peaks at approximately 532 nm and 606 nm are observed associated with d-d transitions due to the crystal field splitting Co^{2+} such that the band $3d^7$ splits up into two sub-bands at 532 nm and 606 nm associated with $Co^{2+} \rightarrow Ti^{4+}$ charge-transfer bands. [28] The broad absorption peak from 700 to 800 nm is related to the green color of cobalt titanates. CoTiO₃ also absorbs light at higher wavelengths in the near infra-red (IR) region from 1,200 to 1,400 nm.
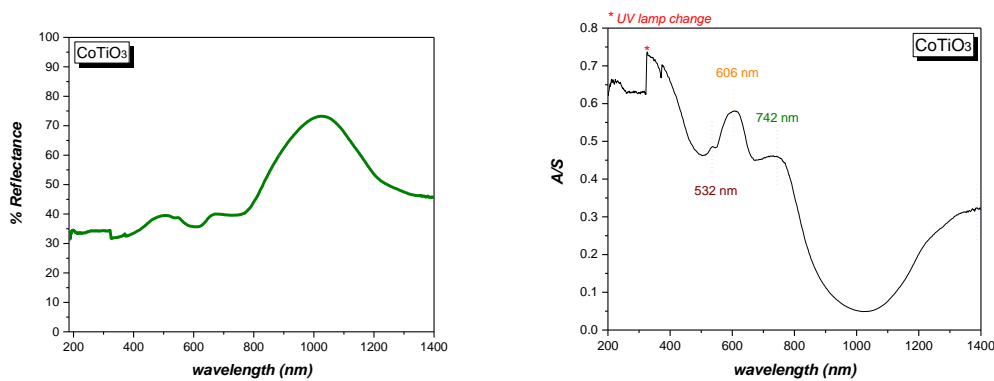
Figure 24. UV-Vis diffuse Reflectance and absorbance spectra of cobalt titanate rods.

The bandgap of CoTiO₃ rods depicted in Figure 25 is estimated from the onset of the absorption edge and is found to be 2.56 eV. Cobalt titanate photocalyst is an indirect transition semiconductor and is able to respond mainly in the visible region of the spectrum.
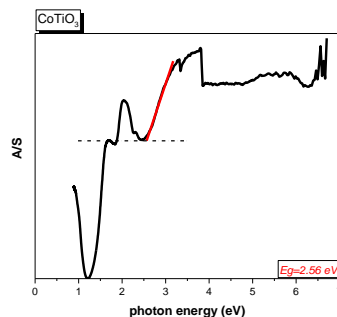

Figure 25. The estimation of bandgap of pure CoTiO₃ rods.

3.1.2.2. Nickel Titanate (NiTiO₃) rods

In order to examine the formation of nickel titanate, different annealing processes took place in low and high temperatures. The molar ratio (see Figure A4) of the metals before and after the annealing was 1:1, as it is depicted in Table 3.

Table 3. The molar ratio between the two metals for all different temperatures.

| Annealing temperature	Atomic % (Ni:Ti)
Before annealing	1:1
400 °C	1:1
500 °C	1:1
600 °C	1:1
800 °C	1:1

The results from the X-ray diffraction are depicted in Figure 26. The as made material is the material before the annealing at high temperatures. The X-ray diffraction pattern of this material corresponds to Ni glycolate (Ni-EG) with the characteristic strong peak located at the low-angle region of approximately 10 ℃. Nickel titanate can not be crystallized in lower or equal temperatures of 400 °C and the PXRD measurements reveal its amorphous phase both at 400 °C and at 500 °C. At 600 °C, nickel titanate has been formed, with high crystallinity revealed by the narrow diffraction peaks. While, at 800 °C, the same phase exists, without any change both in crystallinity and in phase formation. Therefore, the optimal temperature for the formation of nickel titanate was chosen to be the temperature of 600 °C as an intermediate temperature.
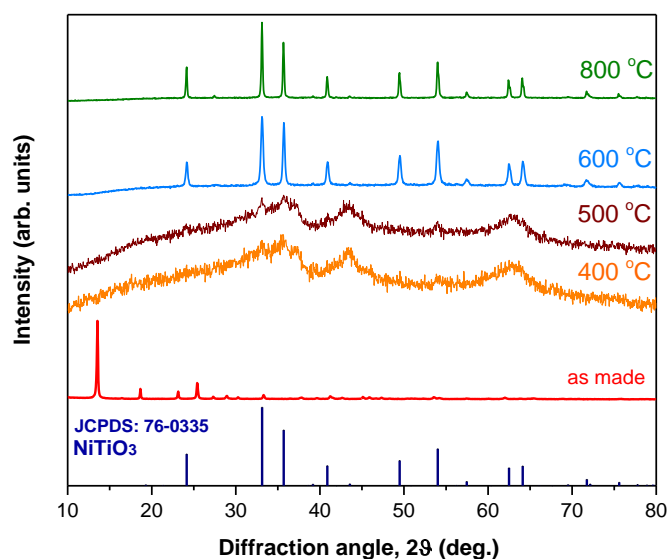
Figure 26. X-ray diffraction pattern of NiTiO₃ before and after annealing at different temperatures.

The characteristic XRD peaks for the annealing temperature of 600 °C are located at angles $2\vartheta = 24.15°, 33.10°, 35.70°, 40.90°, 49.50°, 54.05°, 57.40°, 62.45°, 64.10°, 71.70°, 75.70°$ could be attributed to the $(012), (104), (110), (11\bar{3}), (024), (11\bar{6}),$

$(018), (12\bar{4}), (300), (1010), (220)$ reflections for ilmenite $NiTiO_3$ (JCPDS no. 76-0335). $NiTiO_3$ belongs to the Rhombohedral crystal system, at space group $R\bar{3}$ with space group number 148. No characteristics peaks of other impurities such as TiO_2 or NiO or other phases of nickel titanates are observed. The strong and narrow diffraction peaks reveal the high crystallinity of the prepared powder.
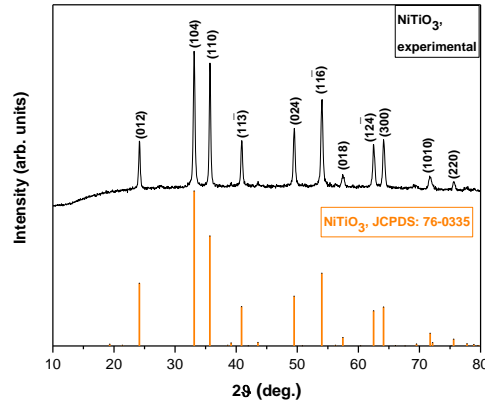

Figure 27. *X-ray diffraction pattern of NiTiO₃ annealed at 600 ᵒC.*

The estimated experimental cell parameters for $NiTiO_3$ at 600 °C are depicted in Table 4 and approximate the theoretical values.

Table 4. *Lattice parameters of NiTiO₃*

NiTiO3	Cell parameters			Angles (degrees)			Volume
	a (Å)	b (Å)	c (Å)	a	β	γ	Å³
theoretical	5.0270	5.0270	13.7880	90	90	120	301.75
experimental	5.0231	5.0231	13.7905	90	90	120	301.3

The morphology of the $NiTiO_3$ powder was observed by SEM, where the rod-like conformation is obvious (Figure 28). The length of the rods is about 1-2 μm and their diameter is about 200 nm.
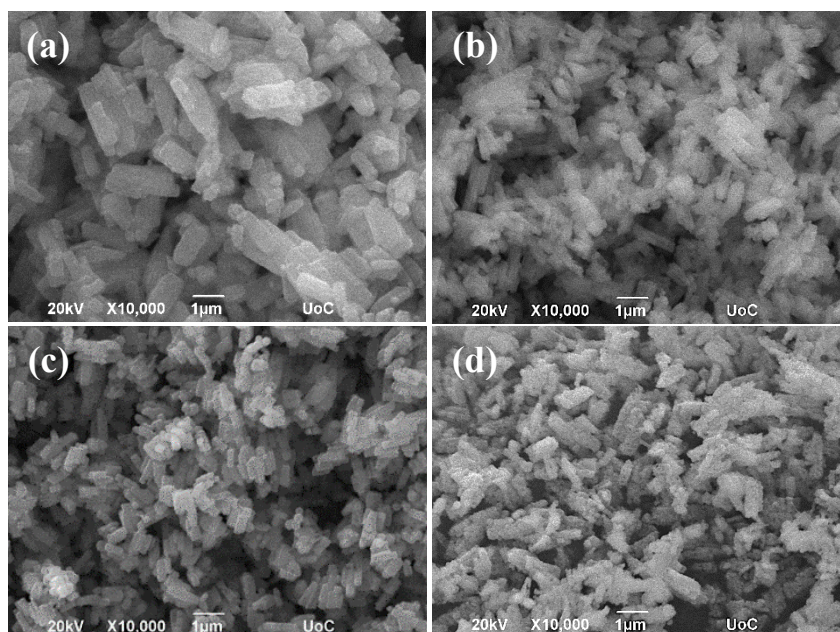
Figure 28. *SEM images of nickel titanate rods (a) before annealing and at different annealing temperatures (b) 400 ºC (c) 600 ºC (d) 800 ºC.*

In Figure 29, the homogeneity of all the individual elements in rods is presented by EDS mapping technique, where the colored dots represent each element.
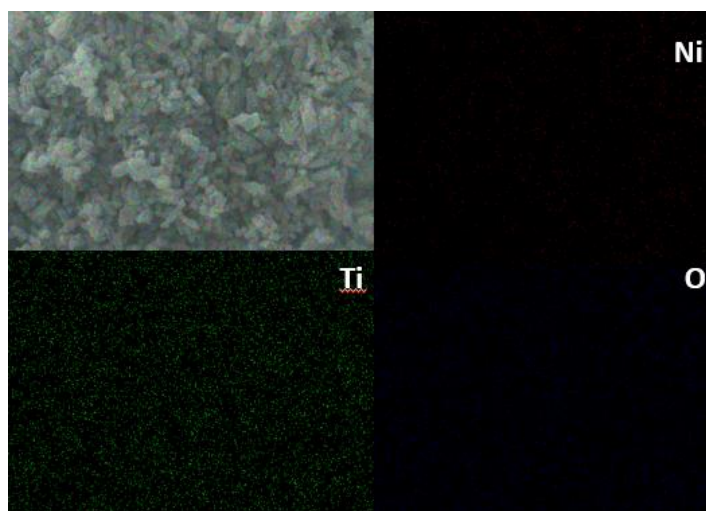
***Figure 29.*** *EDS mapping images of nickel titanate rods.*

In Figure 30, the diffuse reflectance spectrum and the Absorbance/Scattering calculated from the Kubelka-Munk function for nickel titanate are illustrated. From the absorption spectrum, it is shown that $NiTiO_3$ is photo responsive in both UV and visible light ranges. In UV region, the broad absorption edge situated at 410 nm is associated with $O^{2-} \rightarrow Ti^{4+}$ charge transfer interactions and indicates the optical bandgap of nickel titanate. In visible region, there are two absorption bands at approximately 442 nm and 505 nm associated with the d-d transitions due to the crystal field splitting of Ni^{2+} such that the $3d^8$ band associated with Ni^{2+} ions splits up into two sub-bands at approximately 490 nm and 650 nm associated with $Ni^{2+} \rightarrow Ti^{4+}$ charge-transfer bands. [5] At higher wavelengths, the broad intense absorption in the visible region from 600 to 800 nm is associated to the yellow color character of $NiTiO_3$. The peak at 840 nm corresponds to

the electronic transitions of additional energy levels caused by defects and impurities. [61] In addition, nickel titanate absorbs light at higher wavelengths in the near infra-red (IR) region from 1,000 to 1,400 nm, where the additional energy levels from these impurities play an important role in the broad absorption band from red-light to near infrared. [26]
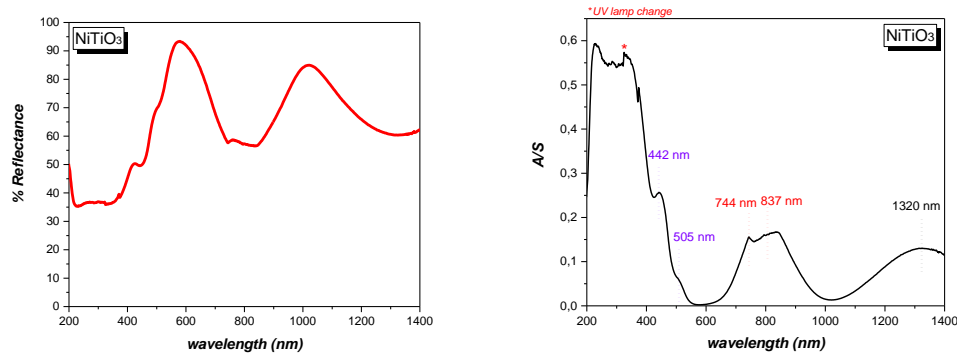
Figure 30. *UV-Vis diffuse Reflectance and absorbance spectra of nickel titanate rods.*

The energy bandgap of $NiTiO_3$ rods was estimated from the onset of the absorption edge and is found to be 3 eV (see Fig. 31).
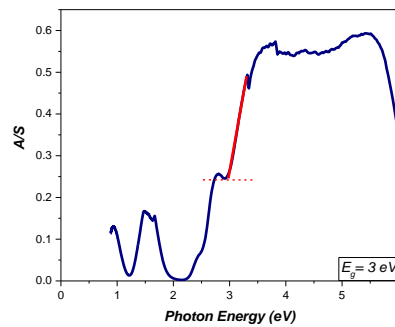
**Figure 31.** *The estimation of bandgap of pure $NiTiO_3$ rods.*

3.1.2.3. Zinc Titanate ($ZnTiO_3$) rods

The EDS measurement for the powder before the annealing process revealed a molar ratio of 1:1 between the two metals of Zn and Ti are depicted in Table 5 (see also Figure A5 in the Appendix section).

Table 5. *The molar ratio between the two metals for all different temperatures.*
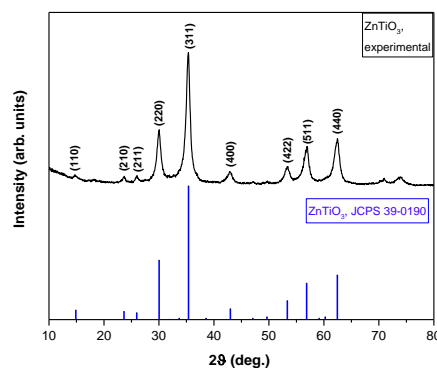
Annealing temperature	Atomic % (Zn:Ti)
Before annealing	1:1
400 °C	1:1
500 °C	1:1
600 °C	1:1
800 °C	1:1

In Figure 32, all the X-ray diffraction patterns for the different annealing temperatures are depicted. The amorphous phase at the temperatures of 400 ºC is revealed. While, a further annealing at 500 ºC, shows that $ZnTiO_3$ has started to be formed. The temperature of 600 ºC is the optimal formation temperature and a further annealing at 800 ºC, reveals that rhombohedral $ZnTiO_3$ has a phase transformation to the hexagonal phase of $ZnTiO_3$, while the rhombohedral phases remains. Therefore, at 800 ºC, the two phases of rhombohedral and hexagonal $ZnTiO_3$ exist.
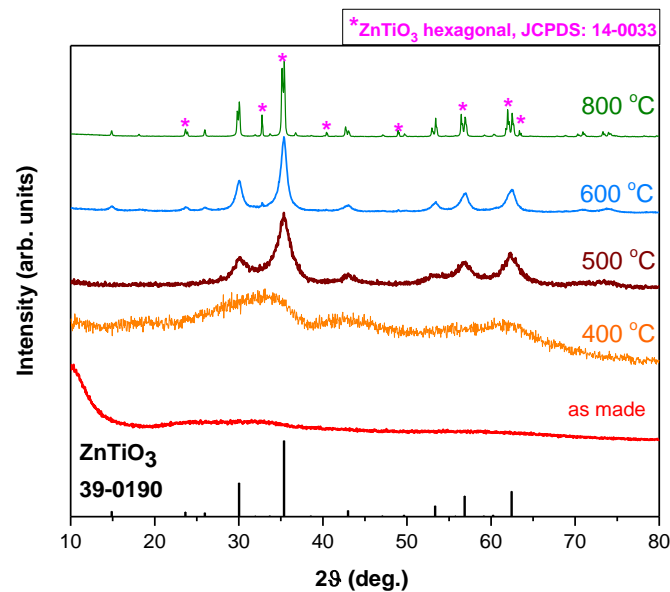

Figure 32. X-ray diffraction pattern of ZnTiO₃ before and after annealed at different temperatures.

In Figure 33, the characteristic XRD peaks at $2\vartheta = 14.70°, 23.70°, 26.00°, 30.05°, 35.35°,$ $42.85°, 53.46°, 56.91°, 62.46°$ could be attributed to the $(110), (210), 9211), (220),$ $(311), (400), (422), (511), (440)$ reflections of cubic ilmenite $ZnTiO_3$. No characteristics peaks of other impurities such as TiO_2 or ZnO are observed. The strong and narrow diffraction peaks reveal the high crystallinity.


Figure 33. X-ray diffraction pattern of ZnTiO₃ annealed at 600 ºC.

The morphology of the ZnTiO$_3$ powder at all different annealing temperatures was observed by SEM, where the rod-like conformation is obvious (see Figure 34). The length of the rods is about 1-2 μm and their diameter is about 200 nm.
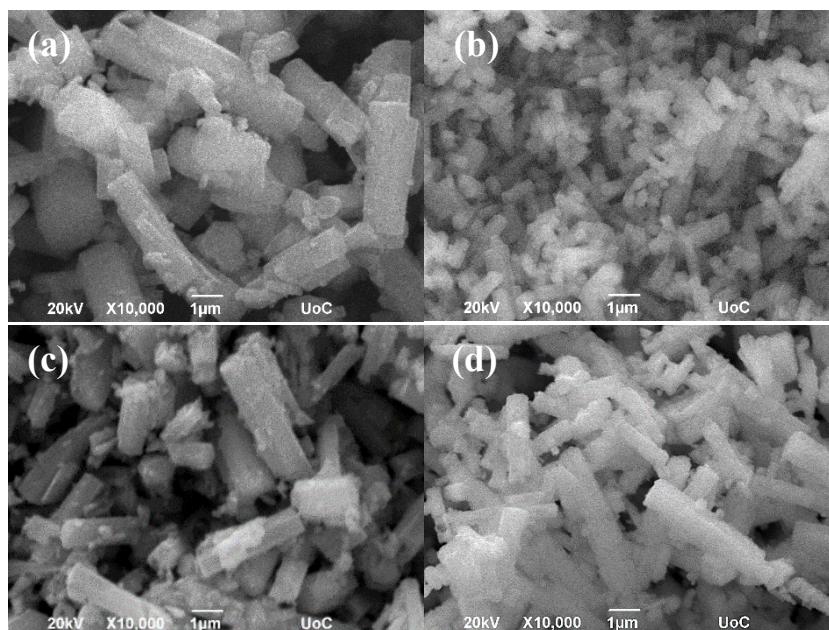

Figure 34. SEM images of zinc titanate rods (a) before annealing and at different annealing temperatures (b) 400 ºC (c) 600 ºC (d) 800 ºC.

In Figure 35, the homogeneity of all the individual elements is presented by EDS mapping technique, where the colored dots represent each element.
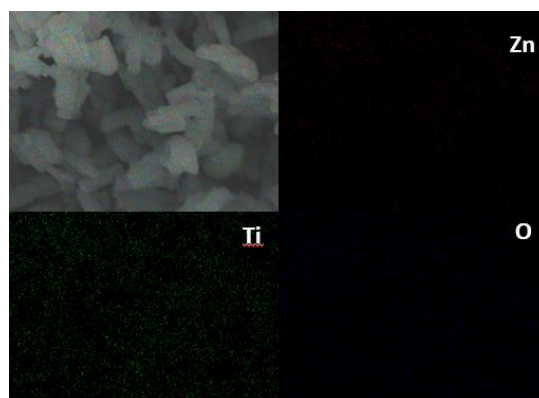

Figure 35. EDS mapping images of zinc titanate rods.

ZnTiO$_3$ demonstrates a photo absorption only in the UV range of the spectrum in Figure 36. In UV region, a broad absorption edge at 352 nm is associated with the optical band gap attributed to the $O^{2-} \rightarrow Ti^{4+}$ charge transfer interactions. In addition, this absorbance explains the bright white color of the power. The bandgap of ZnTiO$_3$ estimated from the onset of the absorption edge is found to be 3.5 eV, thus by corresponding only to UV illumination, zinc titanate is not able to absorb visible light and therefore it seems that the material will not be an active material for solar light applications.
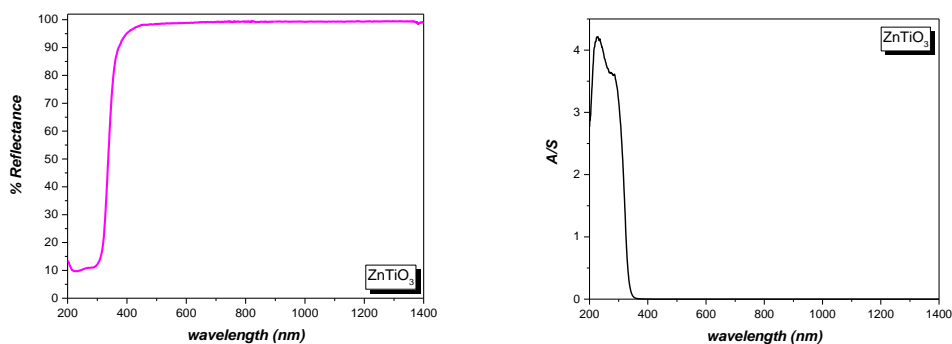
Figure 36. *UV-Vis diffuse Reflectance and absorbance spectra of zinc titanate rods.*
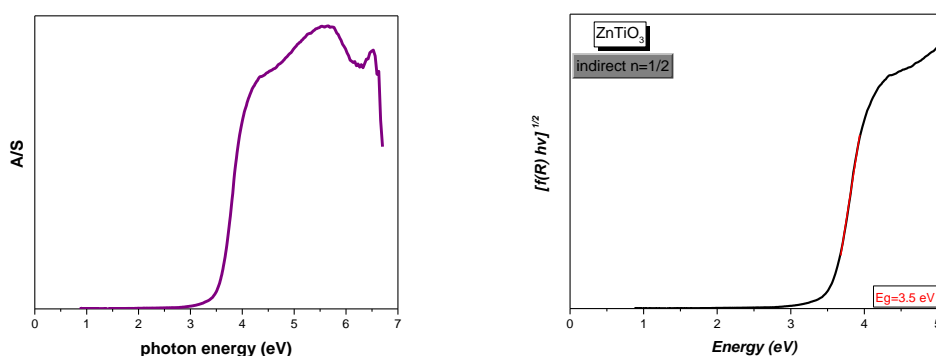
Figure 37. *(a) Absorption/Scattering vs energy and (b) the estimation of bandgap of pure ZnTiO₃ rods.*

3.1.2.4. Magnesium Titanate (MgTiO₃) rods

Like in other titanates, the EDS analysis the percentages of each element existing in the rods can be viewed by the EDS analysis (see Figure A6 in the Appendix section), where the ratio Mg:Ti is equal.

Table 6. *The molar ratio between the two metals for all annealing temperatures.*

Annealing temperature	Atomic % (Mg:Ti)
Before annealing	1:1
400 °C	1:1
500 °C	1:1
600 °C	1:1
800 °C	1:1

After the EDS analysis, all the X-ray diffraction patterns were obtained for all different annealing temperatures of magnesium titanates. The as-made pattern corresponds to the powder before the annealing process at high temperatures. This X-ray pattern of the precursor material reveals the peaks of Mg glycolate (Mg-EG) with the characteristic strong peak located at the low-angle region of approximately 10°. The annealing at the temperatures of 400 °C and 500 °C revealed the amorphous phase of the material. The material was formed at the temperature of 600 °C, with high and narrow peaks to be observed. However, the phase of MgTiO₃ is not pure, with a second phase of MgTi₂O₅

to be appeared. A further annealing at 800 °C, revealed that both the two phases exist, but the crystallinity of the samples increases, possibly due to the higher annealing temperature, the crystal has a higher growth.
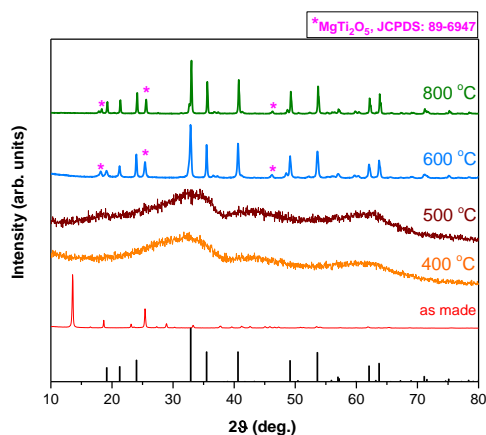
Figure 38. X-ray diffraction pattern of MgTiO₃ annealed at different temperatures.

The structure of the sample was identified using X-Ray diffraction pattern, as it is depicted in figure 38. The characteristic XRD peaks at $2\vartheta = 19.10°, 21.25°, 24.00°, 32.85°, 35.50°, 40.60°, 49.15°, 53.60°, 59.95°, 62.05°, 63.70°, 71.15°, 75.10°$ could be attributed to the $(100), (210), (301), (410), (511), (11\bar{3}), (024), (11\bar{6}), (018), (12\bar{4}), (300), (1010), (220)$ reflections for ilmenite MgTiO₃ (JCPDS card number 79-0831). A second phase of magnesium titanate is also observed and belongs to the MgTi₂O₅ crystal phase. The characteristic peaks of the second phase appear at $2\vartheta = (18.15°), (25.40°), (46.20°)$ and could be attributed to the $(200), (101), (430)$ reflections for MgTi₂O₅ (JCPDS card number 89-6947). MgTiO₃ belongs to the Rhombohedral crystal system, at space group $R\bar{3}$ with space group number 148. Whereas, MgTi₂O₅ belongs to the Orthorhombic crystal system, at space group Bbmm, with space group number 63. No characteristics peaks of other impurities such as TiO₂ or MgO are observed. The strong and narrow diffraction peaks reveal the high crystallinity. The lattice parameters were calculated and depicted in Table 7.
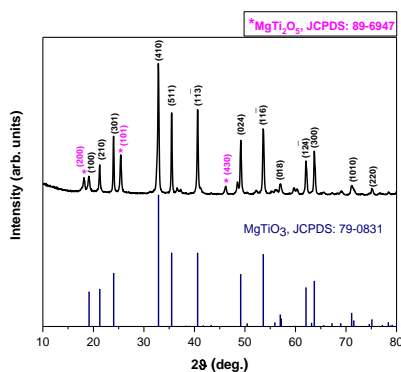

*Figure 39. X-ray diffraction pattern of MgTiO₃ annealed at 600 °C.*

Table 7. *Lattice parameters of MgTiO₃*

Table 7. *Lattice parameters of MgTiO₃*

MgTiO₃	Cell parameters			Angles (degrees)			Volume
	a (Å)	b (Å)	c (Å)	a	β	γ	Å³
theoretical	5.0476	5.0476	13.8912	90	90	120	307.5069
experimental	5.0523	5.0523	13.9064	90	90	120	307.4

The morphology of the MgTiO₃ sample was revealed by SEM observations, where the rod-like conformation is obvious. The length of the rods is about 400 nm and their diameter is about 200 nm. In addition, the homogeneity of the individual elements in rods is presented by EDS mapping (Fig.41).
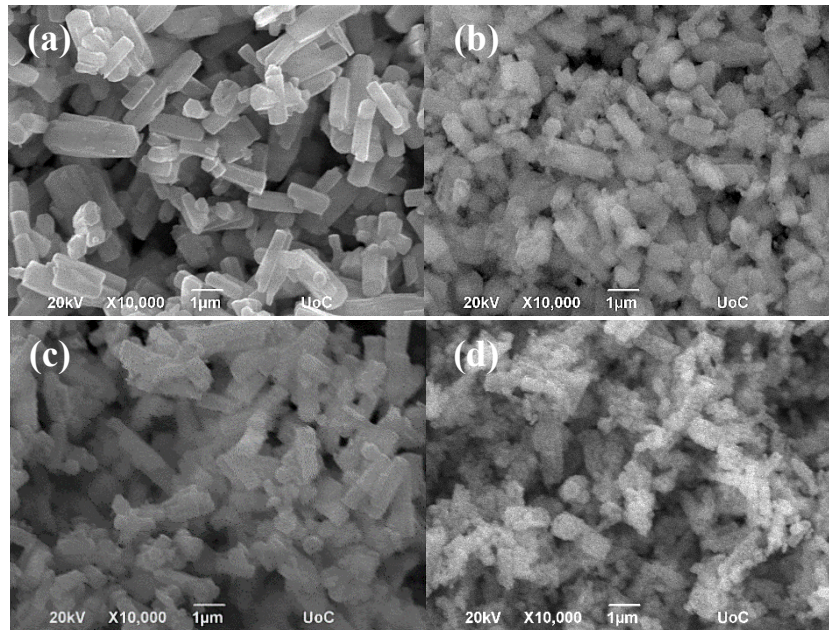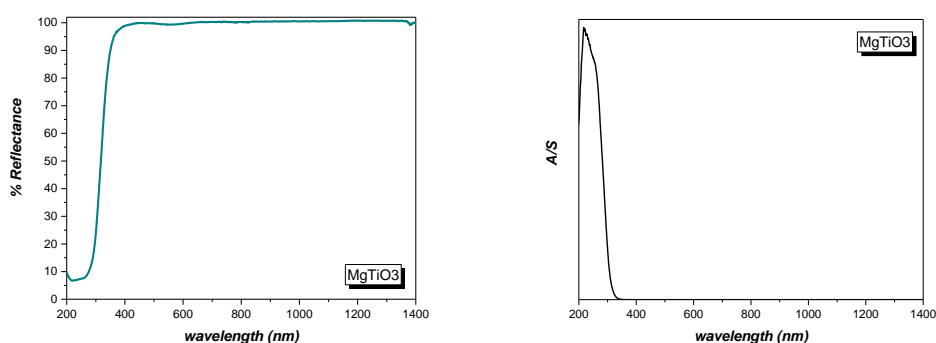

Figure 40. *SEM images of magnesium titanate rods (a) before annealing and at different annealing temperatures (b) 400 ºC (c) 600 ºC (d) 800 ºC.*
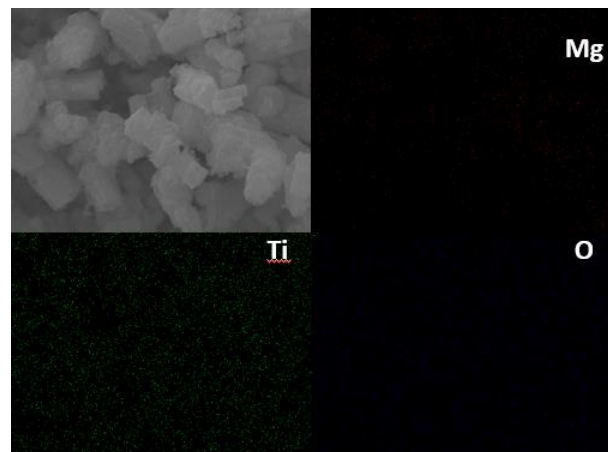

Figure 41. *EDS mapping images of magnesium titanate rods.*

MgTiO₃ reveals absorption bands at wavelengths lower than 400 nm, as it is illustrated in Figure 42, explaining the bright white color of powder. The broad absorption edge of MgTiO₃ is found in the UV region ($\lambda <$ 400nm) at 330 nm, associated with $O^{2-} \rightarrow Ti^{4+}$ charge transfer interactions and indicates the optical bandgap of magnesium

titanate. Therefore, the corresponding bandgap calculated from the onset of the absorbance edge of the material is 3.7 eV (see Figure 43), indicating a wide band semiconductor with restricted absorbance in visible region. [13]

Figure 42. *UV-Vis diffuse Reflectance and absorbance spectra of magnesium titanate rods.*
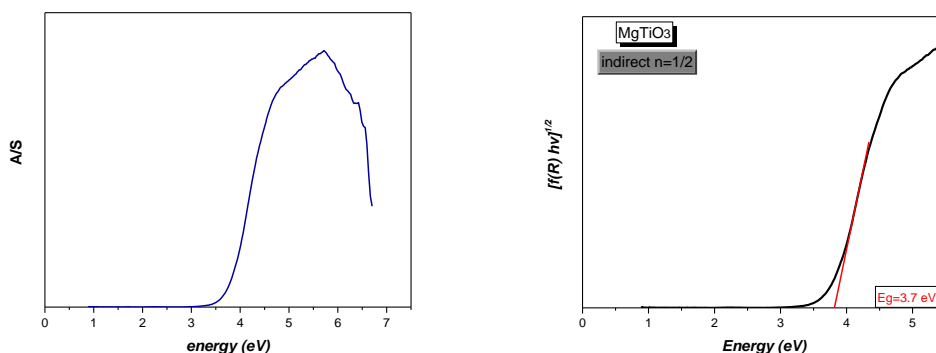
Figure 43. *(a) Absorption/Scattering vs energy and (b) the estimation of bandgap of pure MgTiO₃ rods.*

3.1.3 Photocatalytic experiments of metal titanates towards H_2 production

As already has been mentioned in the introduction, metal titanates are not active materials for photocatalytic water splitting towards H_2 production. $NiTiO_3$ and $CoTiO_3$ have unsuitable band edges for H_2 production and $MgTiO_3$ and $ZnTiO_3$ have wide bandgaps and can be activated only in UV spectrum. [54] Nevertheless, they were tested for photocatalytic water splitting in order to be used as reference samples for the following experiments of the combined materials and none of them was an active photocatalyst for H_2 evolution.
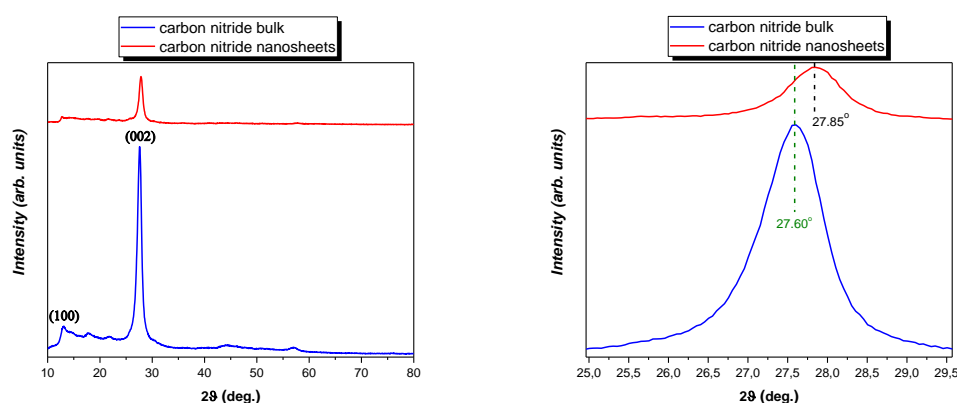
3.2 Carbon nitride nanosheets (CNNs)

3.2.1 Preparation of carbon nitride nanosheets (CNNs)

CNNs were obtained with a modified post-thermal oxidation etching technique. [41] Melamine was used as a precursor material and after the first step of calcination, polymeric carbon nitride bulk was obstained. In this step it has to be mentioned that melamine was covered with an aluminum foil in order to not react with air during the

annealing process. The second step involves the annealing of carbon nitride bulk in air, which provides carbon nitride bulk with groups of oxygen. After the annealing, the formed CNNs is a porous and lightweight material. It has to be mentioned that the annealing processes took place in a very low rate (2 $^{\circ}$C/min was the increment rate of temperature and left to cool down to room temperature). The production of the carbon nitride bulk from melamine has a mass yield of approximately 50% and the production of CNNs from bulk has a mass yield of 10%.

3.2.2 Morphology, structural and optical properties

The low-angle reflection peak at $2\vartheta = 13°$ corresponds to the in-plane repeats between tri-s-triazine units, while the strongest peak at $2\vartheta = 27.6°$ corresponds to the periodic interlayer stacking of the conjugated aromatic system (see Figure 44). Compared to the peak at the $2\vartheta = 27.6°$ of PCN bulk, the intensity peak in nanosheets is much weaker due to the thermal oxidation etching of bulk carbon nitride by the annealing process. This is mainly attributed to the damage of the interlayer stacking of the repeated packing of aromatic rings in PCN, namely, there are less united sheets which is a typical feature of porous PCN. The shift in the angles from 27.6° to 27.85° is related to the lower interplanar distance d. We suggest that the lower interplanar distance d, has occurred due to the thermal treatment, when the H_2 atoms existing in heptazines were removed. Indicatively mentioned the interplanar distances d for bulk and nanosheets, calculated from the Bragg's low equation; d_{CNB}=3.23 Å > d_{CNNs}=3.20 Å. The unique peak in the PXRD graph of CNNs can explain that is a 2-D material. [41]


Figure 44. *X-ray diffraction pattern of carbon nitride bulk and nanosheets.*

In Figures 45 and 46, SEM images of carbon nitride bulk and nanosheets are depicted. Carbon nitride bulk is an amorphous material, consists of unhmogeneous morphology with no specific shape. It seems that CNNs consist of smaller sheets compared to bulk.
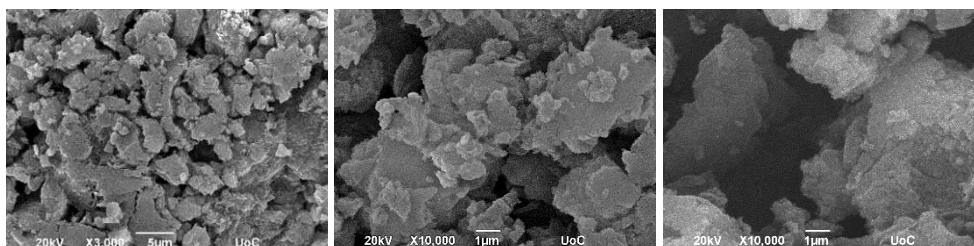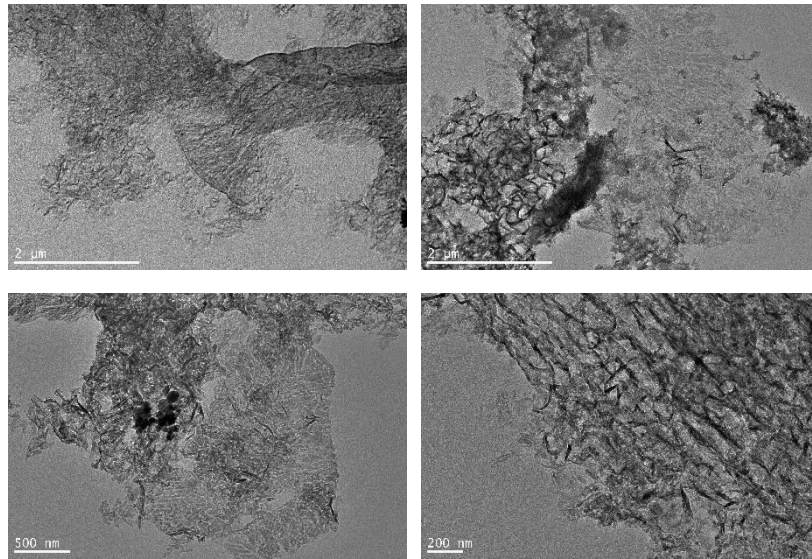

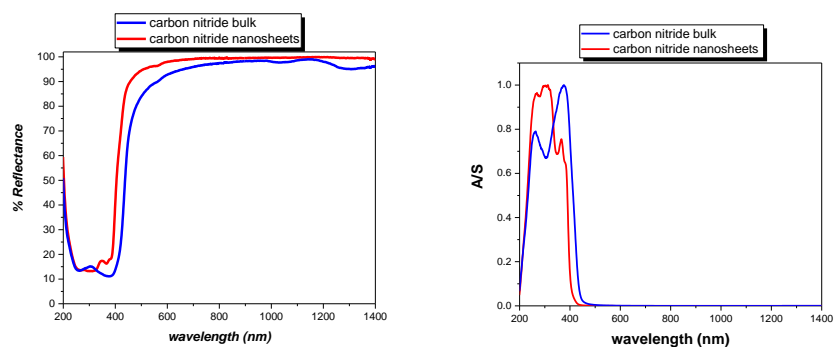**Figure 45.** *SEM images of carbon nitride bulk.*
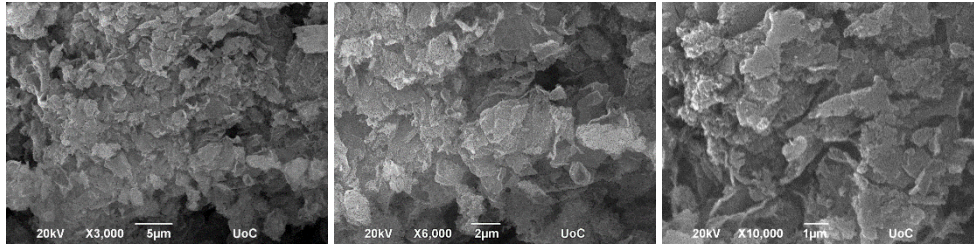
***Figure 46.** SEM images of CNNs.*

The shape of CNNs can be obvious from the SEM images, as TEM is the appropriate technique to observe 2D materials. In Figure 47, TEM images for the exfoliated carbon nitride are represented and reveal the lateral size of the sheets which is approximately some μm and their nano-metric size thickness.


***Figure 47.** TEM images of CNNs.*

In Figure 48, a blue shift of the intristic absorption edge is observed to the CNNs compared to bulk. The bandgap of carbon nitride bulk is estimated to be 2.7 eV, showing an absorption in the blue region of the visible spectrum, verified to the yellow color of the powder of carbon nitride bulk. In addition, the bandgap of CNNs is calculated to be 2.9 eV, estimated from the onset of the absorption edge, verified also from the light yellow color of nanosheets' powder. The calculated bandgap of the nanosheets is higher than the bandgap of the bulk material, something that it was expected due to the quantum confinement effect, that conduction and valence band move to opposite directions.

Figure 48. *UV-Vis diffuse Reflectance and absorbance/scattering spectra of carbon nitride bulk and nanosheets.*
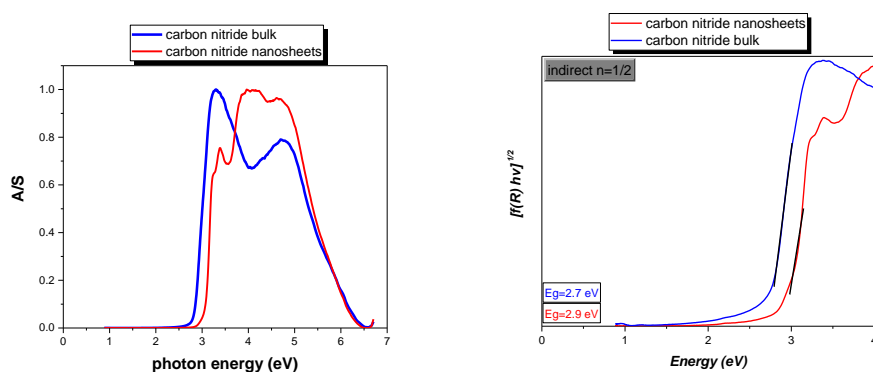
Figure 49. *The estimation of bandgap of carbon nitride bulk and nanosheets.*

3.2.3 Photocatalytic experiments of CNNs towards H₂ production

The photocatalytic activity of CNNs is equal to 0.71 μmol/h as it is illustrated in Figure 50. As it was expected, the evolved H_2 production rate is not high, due to the low quantum efficiency of CNNs. This low efficiency was attributed to charge recombination and the short lifetime of the photogenerated electrons and holes. [40]
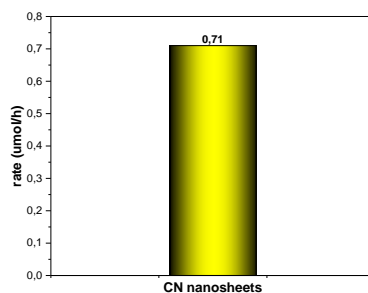
Figure 50. *Photocatalytic H₂ evolution using CNNs under UV/Vis illumination.*

3.3 Combination of metal titanate rods with carbon nitride sheets

### 3.3.1 Dispersion of metal titanates and CNNs in isopropanol

The combination of metal titanates rods with CNNs followed by a simple sonication technique. Firstly, the powders were dispersed in various solvents in order to find out

the solvent where the powder could have the optimal dispersion. The solvents that were used are: ethanol, methanol, isopropanol and water. It was observed that both metal titanates and CNNs displayed the best dispersion in isopropanol.

## 3.3.2 Morphology, structural and optical properties of the heterojunctions

3.3.2.1 Nickel Titanate (NiTiO₃) rods with CNNs

In order to find out the most suitable material for the creation of the heterostructure between nickel titanate rods and CNNs, a series of different combinations were synthesized. By combining nickel titanate with a small amount of CNNs, the changes in the XRD graph and SEM images were not obvious (see Figure A7 and A8 in the Appendix section). Therefore, an intermediate concentration of all the different combinations, adjusted to $NiTiO_3$ – 4 wt% CNNs was chosen in order to be tested for photocatalytic water splitting and studied further. In addition, another two materials were synthesized; $NiTiO_3$ – 10 wt% CNNs and $NiTiO_3$ – 50 wt% CNNs, in order to examine which is the optimal concentration of CNNs for the activation of photocatalyst nickel titanate rods.
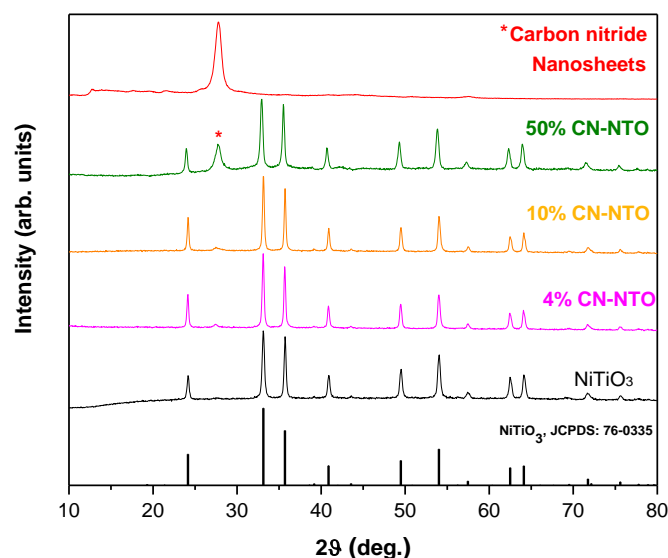
***Figure 51.** X-ray diffraction pattern of NiTiO₃ combined with CNNs.*

The combination of nickel titanate rods with CNNs at different concentrations are illustrated in the following figures. For the concentrations of $NiTiO_3$ – 4 % CNNs and $NiTiO_3$ – 10 wt% CNNs there is not an obvious difference in structure or in morphology. However, in the SEM pictures of the material $NiTiO_3$ – 50 wt% CNNs, the morphology has changed and CNNs appear clearly in the picture.
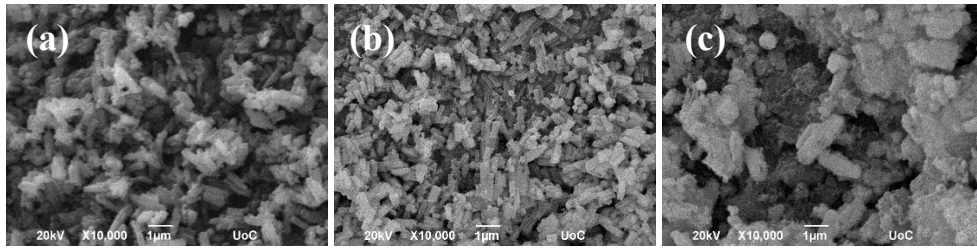
Figure 52. *SEM images of NiTiO₃ with (a) 4 wt% CNNs, (b) 10 wt% CNNs, (c) 50 wt% CNNs.*

Remarkably, the combination of CNNs with NiTiO₃, resulted in the band edge shifting to longer wavelengths by increasing the amount of CNNs.

From the Figure 53, it can be seen that the absorption band edge of NiTiO₃ – 4 wt% CN is approximately at 430 nm, resulting to a bandgap of 2.8 eV.
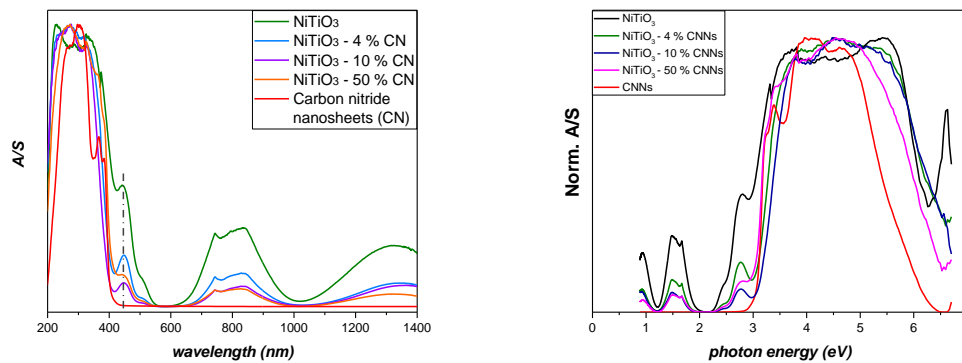
Figure 53. *Absorbance spectra and calculation of the band gap of composite materials.*

All the estimated values for the composite materials are depicted in the table 8. The energy bandgap values of the composite materials revealed intermediate values between the two individual photocatalysts.

Table 8. *Band gap values of composite materials.*

photocatalyst	Energy gap (eV)
NiTiO₃	3.0
NiTiO₃ – 4% CNNs	2.8
NiTiO₃ – 10% CNNs	2.9
NiTiO₃ – 50% CNNs	2.8
CNNs	2.9

3.3.2.2 Cobalt Titanate (CoTiO₃) rods with CNNs

In order to find out the most suitable material for the creation of the heterostructure between cobalt titanate rods and CNNs, a series of different combination was created. By combining cobalt titanate with a small amount of CNNs, the changes in the XRD graph and SEM images are not obvious (see Figure A9 and A10 in the Appendix section). Therefore, the intermediate concentration of CoTiO₃ – 4 wt% CNNs was chosen in order to be tested for photocatalytic water splitting and studied further.

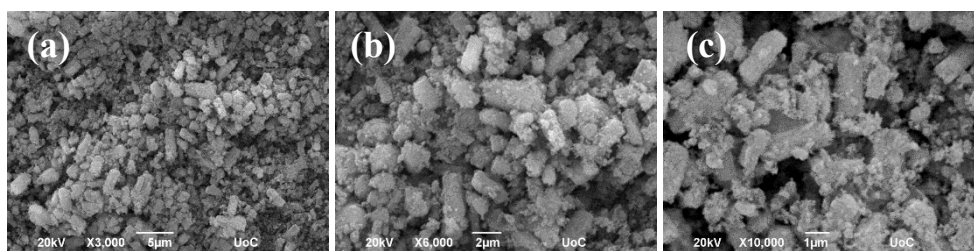*Figure 54. SEM images of CoTiO₃ – 4 wt% CNNs.*

The combination of cobalt titanate with CNNs took place in order to attempt to activate cobalt titanate rods for H₂ production because its unsuitable band edges make it an inactive material for photocatalytic water splitting. From the Table 9, it can be seen that the absorption band edge of CoTiO₃ – 4 wt% CN is approximately at 480 nm, resulting to a bandgap of 2.65 eV. The benefit of this heterostructure is that absorbs at the visible light of the solar spectrum.
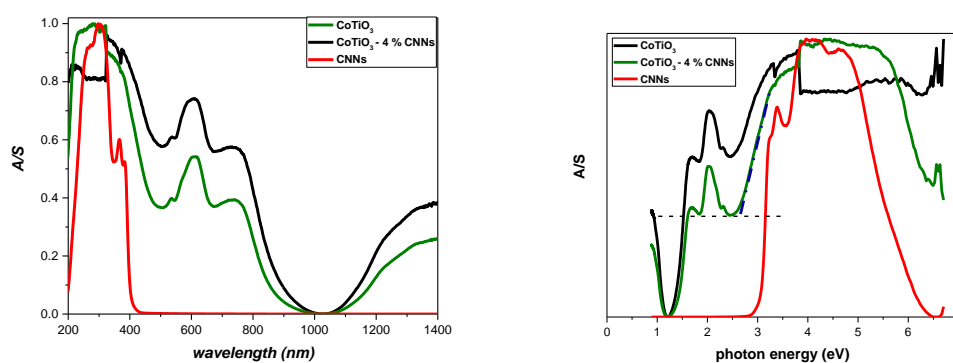

Figure 55. Absorbance spectra and calculation of the band gap of CoTiO₃ – 4 wt% CNNs.

Table 9. Band gap values of CoTiO₃ – 4 wt% CNNs.

photocatalyst	Energy gap (eV)
CoTiO₃	2.56
CoTiO₃ – 4 wt% CNNs	2.65
CNNs	2.9

3.3.2.3 Zinc Titanate (ZnTiO₃) rods with CNNs

A small concentration of CNNs was chosen to be combined with zinc titanate rods in order to test if this metal titanate material can be activated by CNNs. This change is not obvious again neither in the XRD graph, nor in SEM images.

44
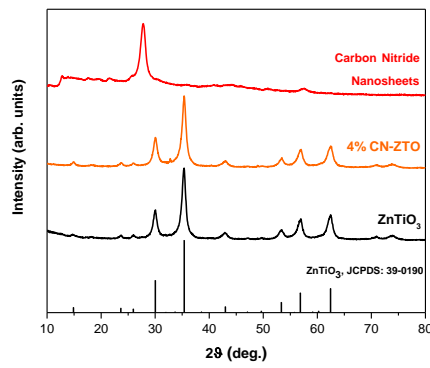
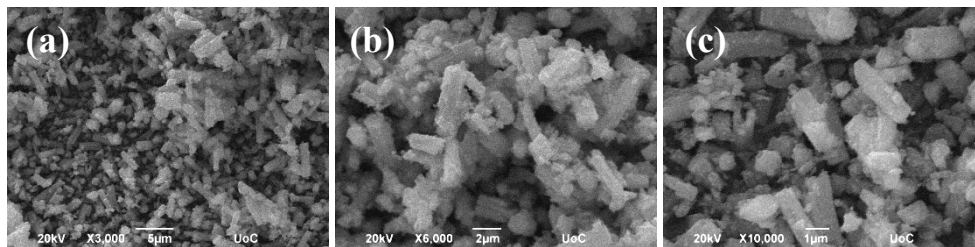*Figure 56. X-ray diffraction pattern of ZnTiO₃ – 4 wt% CNNs.*

In Figure 57, SEM images of ZnTiO₃ – 4 wt% CNNs are illustrated in different magnifications. The morphology of the sample is rod-like, while CNNs can not be distinguished due to their low concentration in the sample.

Figure 57. SEM images of ZnTiO₃ – 4 wt% CNNs.

The combination of zinc titanate with CNNs is essential in order to improve ZnTiO3 photocatalytic activity by activating it with solar energy. In the Figure 58, it can be seen that the absorption band edge of ZnTiO3 – 4 wt% CN is approximately at 370 nm. It seems that by combining these two materials, the absorbance became higher due to the CNNs. However, the combination of zinc titanate with CNNs still lacks the absorption in the visible area. The estimated bandgap of ZnTiO3 – 4 wt% CN is 3.3 eV. Namely, this specific amount of CN's introduction does not shift the absorption in the visible range.
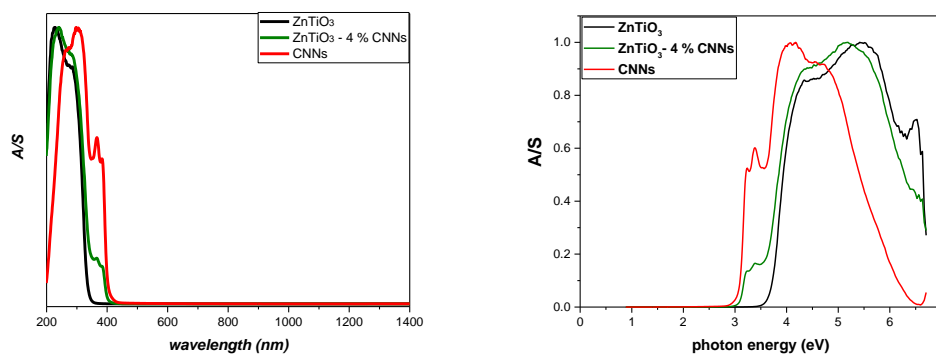
*Figure 58. Absorbance spectra and calculation of ZnTiO₃ – 4 wt% CNNs compared to the individual materials.*

| photocatalyst	Energy gap (eV)
ZnTiO$_3$	3.5
ZnTiO$_3$ – 4 wt% CNNs	3.3
CNNs	2.9

3.3.2.4 Magnesium Titanate (MgTiO₃) rods with CNNs

In the following graph, the X-ray diffraction patterns of magnesium titanate rods, CNNs and their combinations are illustrated. It is obvious that for concentrations lower to 10 wt% of CNNs, the peaks of CNNs are not obvious in the graph but the material MgTiO$_3$ – 50 wt% CNNs presents peaks from both MgTiO$_3$ and CNNs.
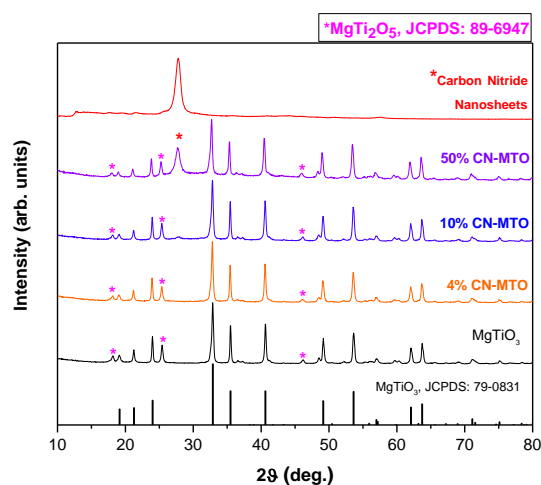
Figure 59. *XRD pattern of MgTiO₃ combined with different concentrations of CNNs.*

In Figure 60, SEM images of MgTiO$_3$ – 4 wt% CN and MgTiO$_3$ – 10 wt% CNNs are illustrated. The morphology of the sample is rod-like, CNNs can not be distinguished due to their low concentration in the sample. However, in the powder MgTiO$_3$ – 50 wt% CNNs, both the rods and the sheets can be distinguished.
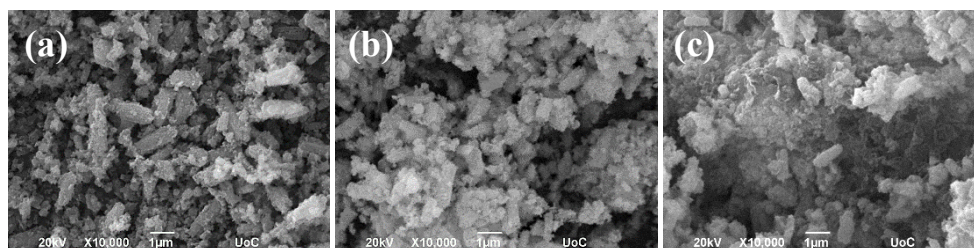
Figure 60. *SEM images of MgTiO₃ with (a) 4 wt % (b) 10 wt% and (c) 50 wt% CNNs.*

The powder MgTiO$_3$–10 wt% CNNs was examined by TEM (Figure 61). The morphology of MgTiO$_3$ has a rod-like conformation as it was depicted from the SEM images with a diameter of approximately 200 nm and a length of approximately 500 nm to 1 μm.

We suggest that in the TEM image 61 (a) the connection between the $MgTiO_3$ with CNNs seems to has been achieved. In addition, in picture 61 (b), the pores of titanate are represented and it is clear that the rods is consisted of smaller nanoparticles, but in addition that there are regions in the sample that $MgTiO_3$ is not connected with CNNs, such as in this picture. This is attributed to the low weight% of CNNs in the combination. In images 61 (c) the connection of $MgTiO_3$ with CNNs is also present. In addition, the image 61 (e) shows the polycrystallinity of the sample.
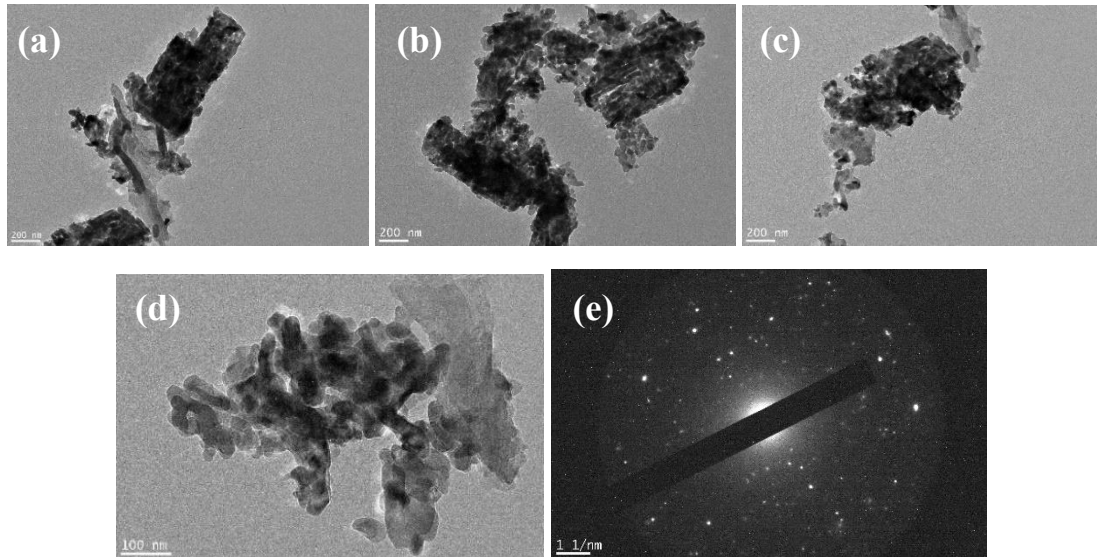
Figure 61. TEM images and SAED pattern of MgTiO₃ – 10 wt% CNNs.

$MgTiO_3$ reveals absorption bands at wavelengths lower than 400 nm, as it is illustrated in Figure 62, while CNNs reveals an absorption edge at 430 nm. The combination of $MgTiO_3$ with CNNs enhanced the absorbance of materials in visible region. As illustrated in Figure 62, by increasing the percentage of CNNs, the absorbance of the different materials, is also increasing. The calculated bandgaps indicated a lower bandgap or the composite materials compared to pure $MgTiO_3$. In Table11, the estimated values of energy bandgap of all photocatalysts are presented, where it is depicted that the materials with the intermediate concentrations, have also an intermediate energy bandgap regarding the two individual materials.
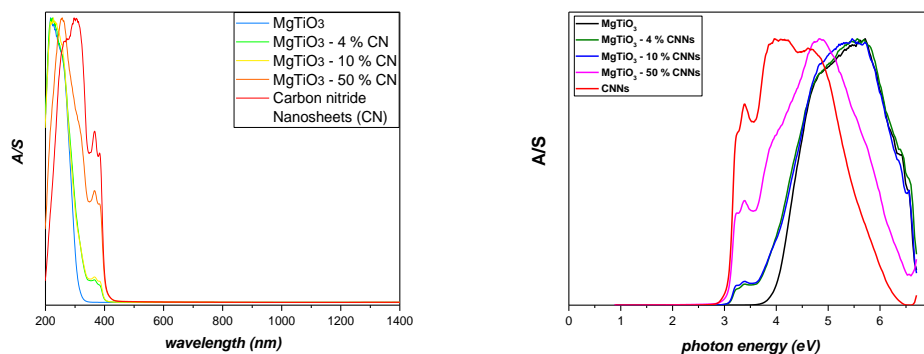

Figure 62. Absorbance spectra and calculation of the band gap of MgTiO₃ combined with CNNs at different concentrations.

Table 11. *Band gap values of MgTiO₃ combined with CNNs.*

photocatalyst	Energy gap (eV)
$MgTiO_3$	3.7
$MgTiO_3$ – 4 wt% CNNs	3.3
$MgTiO_3$ – 10 wt% CNNs	3.2
$MgTiO_3$ – 50 wt% CNNs	2.9
CNNs	2.9

3.3.3 Photocatalytic experiments towards H₂ production

$NiTiO_3$ does not have the appropriate conduction band in order to start the chemical reactions towards H_2 production. By combining it with CNNs, it seems that its photocatalytic behavior does not enhance. The material $NiTiO_3$ – 4 wt% CNNs seemed to be active, but its H_2 production rate is still too low, indicating that the combination with a material that has the appropriate conduction band minimum does not make the metal titanate an active material for photocatalytic water splitting.
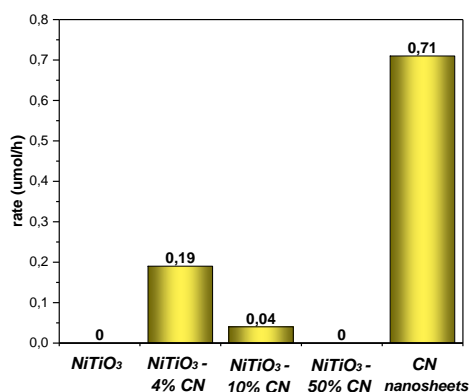
Figure 62. *NiTiO₃ combined with CNNs at different concentrations.*

By inserting CNNs in CoTiO₃, the initial zero production rate of metal titanate is enhanced but only a very small H_2 rate is obtained again.
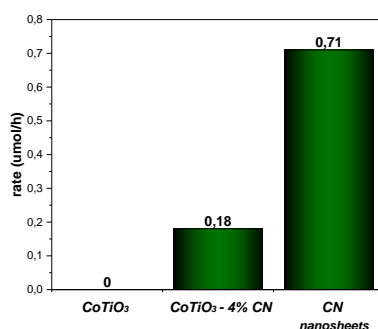
Figure 63. *CoTiO₃ combined with CNNs at different concentrations.*

The combined material of zinc titanate and CNNs is still not active. Since zinc titanate has the appropriate band edges for H_2 production, the reason for its inactivity could be attributed to its wide bandgap that cannot be activated with the visible light illumination.
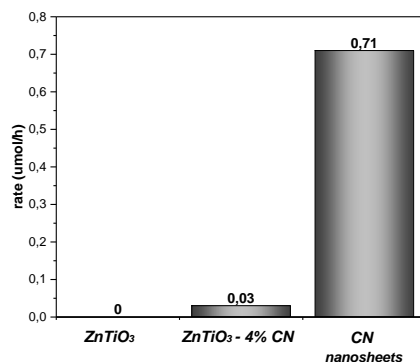

Figure 64. ZnTiO$_3$ combined with CNNs at different concentrations.

Magnesium titanate combined with 10 wt% CNNs is the most active material for H_2 production of all materials created in this work. Nevertheless, its performance is still too low; only 1 μmol/h of H_2 was produced. The wide bandgap of the material could be a reason for this low performance, as this material can not exploit visible light and is active only by UV illumination. The combination of metal titanate with higher concentrations of CNNs seems to have a negative impact in its photocatalytic performance. The higher amount of CNNs could perform as centers of recombination of photogenerated electrons – hole pairs, reducing its photocatalytic performance.
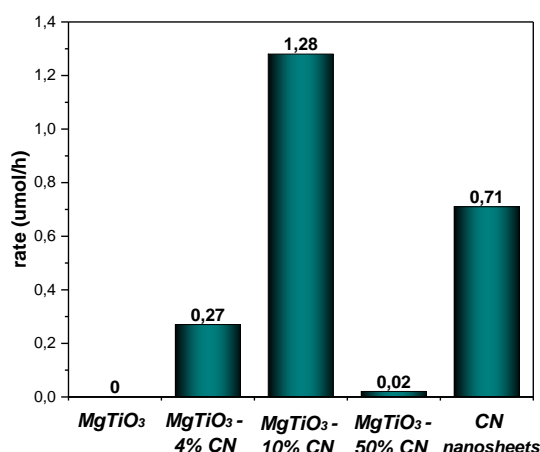
Figure 65. MgTiO$_3$ combined with CNNs at different concentrations for photocatalytic water splitting

Chapter 4 – Conclusions and Perspectives

Conclusions

The synthetic mechanism for the formation of metal titanates was based on a sol-gel method modified from the literature. A parametric study regarding the synthetic procedure took place and revealed that at acidic pH, the rods can not be formed and the material has an amorphous phase, while at neutral and alkaline pH the rods were formed. The structure of the materials was identified by PXRD measurements and the morphology of the powders was examined by SEM and TEM measurements, where the powders revealed a rod-like conformation with a length of 1-2 μm and a diameter of approximately 200 nm. The UV-Vis analysis revealed the energy gap of the materials, with $CoTiO_3$ ($E_g= 2.56$ eV) and $NiTiO_3$ ($E_g= 3$ eV) corresponded to visible light, while $ZnTiO_3$ and $MgTiO_3$ had a strong absorption to UV light and energy gaps values of 3.5 and 3.7 eV respectively. The energy gap of $MgTiO_3$ and $ZnTiO_3$ was attributed to the O^{2-} to Ti^{4+} transition, while the A/S graphs revealed the d-d transitions between the metals in the samples of $CoTiO_3$ and $NiTiO_3$.

The preparation of CNNs was a two-step annealing process, where the annealing temperature and its increment rate were two significant parameters in the final obtained powder. The X-ray diffraction measurement revealed the formation from bulk to CNNs, with the much weaker intensity of the dominant peak, due to the exfoliation from thermal oxidation from the bulk material to CNNs. SEM images revealed the amorphous phase of carbon nitride bulk. TEM images of the CNNs revealed that the porous material was consisted of sheets with nanometric thickness and micrometric lateral size. The optical measurements for carbon nitride bulk and CNNs revealed the blue shift of the CNNs compared to bulk and the higher energy gap of CNNs was attributed to the quantum confinement effect, where the valence and conduction band move to opposite directions. Both the two materials have a strong absorption to UV and to a part of visible range of the solar spectrum. Regarding the photocatalytic experiments, the H_2 production rate of CNNs was not high as it was anticipated from literature.

The preparation of the heterostructure between metal titanates and CNNs was prepared through a sonication process and a further annealing in order to ensure the connection of the two individual materials. A series of different weight% concentrations was prepared, characterized by SEM, TEM and UV-Vis spectroscopy. The heterostructured materials containing metal titanates and CNNs proved to have a low H_2 production rate through water splitting, under solar light illumination. Although $MgTiO_3$ and $ZnTiO_3$ had the appropriate conduction band edges, their band gap could not respond to visible light illumination even after their combination with CNNs. Therefore, their low efficiency may be attributed to their wide band gaps that can exploit only the 4% of the solar spectrum. In addition, $NiTiO_3$ and $CoTiO_3$ did not have the appropriate conduction band edge and their combination with CNNs, although targeted to the transfer of the electrons from titanate to carbon nitride in order to initiate the chemical reaction towards H_2 production, did not optimize their photocatalytic behavior. The

material was the highest H_2 production proved to be the MgTiO$_3$ – 10 wt% CNNs. TEM images revealed that the individual materials were connected in order to create a heterostructure, but also there were regions with pure MgTiO$_3$, which was attributed to the low weight% of CNNs in the combination.

Perspectives

NiTiO$_3$ and CoTiO$_3$ could be studied as potential photocatalysts for oxygen (O_2) evolution due to their suitable valence band edge for the oxidation of water.

MgTiO$_3$ and ZnTiO$_3$ absorb strongly in the UV-region and combined with a heterostructure with a photocatalyst with more narrow energy band gap than CNNs, could potentially exploit more visible light. In addition, modifications with loading of metals with trap states in the wide energy bandgap of titanates, could result in a narrow bandgap and could increase their photocatalytic activity.

The loading of Pt of the samples could be studied, but it is not a useful approach for scale-up applications.

The impact of the different morphologies, shapes, and crystalline assemblies could be studied, since these factors affect the photocatalytic activity.

The relationship between the bulk materials and their nanoscale counterparts could be studied, since in nanoscale the surface area is increased and there are more active sites for photocatalytic reactions.

Chapter 5 – References

[1] M. A. Ruiz Preciado, A. Kassiba, A. Morales-Acevedo, and M. Makowska-Janusik, "Vibrational and electronic peculiarities of NiTiO3 nanostructures inferred from first principle calculations," *RSC Adv.*, vol. 5, no. 23, pp. 17396–17404, 2015.

[2] I. Shindo, "(The determination of the phase diagram by the slow cooling float zone method (1): the system MgO-TiO2.)," *J. Japanese Assoc. Cryst. Growth*, vol. 8, pp. 1–18, 1981.

[3] H. Birnbaum and R. K. Scott, "X-Ray Diffraction Studies of the System: Zn2TiO4-NiTiO3," *J. Am. Chem. Soc.*, vol. 72, no. 3, pp. 1398–1399, 1950.

[4] E. S. Kim and C. J. Jeon, "Microwave dielectric properties of ATiO3 (A = Ni, Mg, Co, Mn) ceramics," *J. Eur. Ceram. Soc.*, vol. 30, no. 2, pp. 341–346, 2010.

[5] Y. Qu *et al.*, "Facile preparation of porous NiTiO 3 nanorods with enhanced visible-light-driven photocatalytic performance," *J. Mater. Chem.*, vol. 22, no. 32, pp. 16471–16476, 2012.

[6] N. Zhang *et al.*, "Pure phase orthorhombic MgTi2O5 photocatalyst for H2 production," *RSC Adv.*, vol. 5, no. 128, pp. 106151–106155, 2015.

[7] S. Ghaemifar, M. Rahimi-Nasrabadi, S. Pourmasud, M. Eghbali-Arani, M. Behpour, and A. Sobhani-Nasab, "Preparation and characterization of MnTiO3, FeTiO3, and CoTiO3 nanoparticles and investigation various applications: a review," *J. Mater. Sci. Mater. Electron.*, vol. 31, no. 9, pp. 6511–6524, 2020.

[8] L. Wang, L. Liu, D. Xue, H. Kang, and C. Liu, "Wet routes of high purity BaTiO3 nanopowders," *J. Alloys Compd.*, vol. 440, no. 1–2, pp. 78–83, 2007.

[9] H. Kang, L. Wang, D. Xue, K. Li, and C. Liu, "Synthesis of tetragonal flake-like magnesium titanate nanocrystallites," *J. Alloys Compd.*, vol. 460, no. 1–2, pp. 160–163, 2008.

[10] L. Budigi, M. R. Nasina, K. Shaik, and S. Amaravadi, "Structural and optical properties of zinc titanates synthesized by precipitation method," *J. Chem. Sci.*, vol. 127, no. 3, pp. 509–518, 2015.

[11] Y. S. Chang, Y. H. Chang, I. G. Chen, G. J. Chen, and Y. L. Chai, "Synthesis and characterization of zinc titanate nano-crystal powders by sol-gel technique," *J. Cryst. Growth*, vol. 243, no. 2, pp. 319–326, 2002.

[12] Y. F. Deng, S. Di Tang, L. Q. Lao, and S. Z. Zhan, "Synthesis of magnesium titanate nanocrystallites from a cheap and water-soluble single source precursor," *Inorganica Chim. Acta*, vol. 363, no. 4, pp. 827–829, 2010.

[13] L. Meng, Z. Ren, W. Zhou, Y. Qu, and G. Wang, "MgTiO3/MgTi2O5/TiO2 heterogeneous belt-junctions with high photocatalytic hydrogen production activity," *Nano Res.*, vol. 10, no. 1, pp. 295–304, 2017.

[14] Y. Suzuki and M. Morimoto, "Porous MgTi2O5/MgTiO3 composites with narrow pore-size distribution: In situ processing and pore structure analysis," *J. Ceram. Soc. Japan*, vol. 118, no. 1381, pp. 819–822, 2010.

[15] Y. M. Miao, Q. L. Zhang, H. Yang, and H. P. Wang, "Low-temperature synthesis of nano-crystalline magnesium titanate materials by the sol-gel method," *Mater. Sci.*

Eng. B Solid-State Mater. Adv. Technol., vol. 128, no. 1–3, pp. 103–106, 2006.

[16]   U. O. Bhagwat, J. J. Wu, A. M. Asiri, and S. Anandan, "Synthesis of MgTiO3 Nanoparticles for Photocatalytic Applications," *ChemistrySelect*, vol. 4, no. 3, pp. 788–796, 2019.

[17]   N. Zhang, Y. Qu, K. Pan, G. Wang, and Y. Li, "Synthesis of pure phase Mg1.2Ti1.8O5 and MgTiO3 nanocrystals for photocatalytic hydrogen production," *Nano Res.*, vol. 9, no. 3, pp. 726–734, 2016.

[18]   R. Rajesh Kanna, N. R. Dhineshbabu, P. Paramasivam, V. Rajendran, and R. Yuvakkumar, "Synthesis of geikielite (MgTiO3) nanoparticles via sol-gel method and studies on their structural and optical properties," *J. Nanosci. Nanotechnol.*, vol. 16, no. 7, pp. 7635–7641, 2016.

[19]   L. Wang *et al.*, "Fabrication of MgTiO3 nanofibers by electrospinning and their photocatalytic water splitting activity," *Int. J. Hydrogen Energy*, vol. 42, no. 41, pp. 25882–25890, 2017.

[20]   G. Parthasarathy and S. V. Manorama, "A novel method for synthesizing nano-crystalline MgTiO3 geikielite," *Bull. Mater. Sci.*, vol. 30, no. 1, pp. 19–21, 2007.

[21]   E. N. Bunting, "Phase equilibria in the system SiO2-ZnO-Al2O3," *Bur. Stand. J. Res.*, vol. 8, no. 2, p. 279, 1932.

[22]   S. F. BARTRAM and R. A. SLEPETYS, "Compound Formation and Crystal Structure in the System ZnO-TiO2," *J. Am. Ceram. Soc.*, vol. 44, no. 10, pp. 493–499, 1961.

[23]   O. Yamaguchi, ! "Y," vol. 98, no. May, pp. 97–98, 1987.

[24]   A. Chaouchi, S. d'Astorg, S. Marinel, and M. Aliouat, "ZnTiO3 ceramic sintered at low temperature with glass phase addition for LTCC applications," *Mater. Chem. Phys.*, vol. 103, no. 1, pp. 106–111, 2007.

[25]   metode penelitian Nursalam, 2016 and A. . Fallis, "済無No Title No Title," *J. Chem. Inf. Model.*, vol. 53, no. 9, pp. 1689–1699, 2013.

[26]   Y. Qu *et al.*, "Facile preparation of porous NiTiO3 nanorods with enhanced visible-light-driven photocatalytic performance," *J. Mater. Chem.*, vol. 22, no. 32, p. 16471, 2012.

[27]   D. J. Taylor, P. F. Fleig, and R. A. Page, "Characterization of nickel titanate synthesized by sol-gel processing," *Thin Solid Films*, vol. 408, no. 1–2, pp. 104–110, 2002.

[28]   Y. Qu, W. Zhou, and H. Fu, "Porous cobalt titanate nanorod: A new candidate for visible light-driven photocatalytic water oxidation," *ChemCatChem*, vol. 6, no. 1, pp. 265–270, 2014.

[29]   N. Dharmaraj, H. C. Park, C. K. Kim, H. Y. Kim, and D. R. Lee, "Nickel titanate nanofibers by electrospinning," *Mater. Chem. Phys.*, vol. 87, no. 1, pp. 5–9, 2004.

[30]   Y. J. Lin, Y. H. Chang, W. D. Yang, and B. S. Tsai, "Synthesis and characterization of ilmenite NiTiO3 and CoTiO3 prepared by a modified Pechini method," *J. Non. Cryst. Solids*, vol. 352, no. 8, pp. 789–794, 2006.

[31]   M. A. E. F. Gabal, Y. M. Al Angari, and A. Y. Obaid, "Structural characterization and activation energy of NiTiO3 nanopowders prepared by the co-precipitation and impregnation with calcinations," *Comptes Rendus Chim.*, vol. 16, no. 8, pp. 704–711,

2013.

[32] X. Zhang, B. Lu, R. Li, C. Fan, Z. Liang, and P. Han, "Structural, electronic and optical properties of Ilmenite ATiO3(A=Fe, Co, Ni)," *Mater. Sci. Semicond. Process.*, vol. 39, pp. 6–16, 2015.

[33] M. W. Li, J. P. Yuan, X. M. Gao, E. Q. Liang, and C. Y. Wang, "Structure and optical absorption properties of NiTiO3 nanocrystallites," *Appl. Phys. A Mater. Sci. Process.*, vol. 122, no. 8, pp. 1–7, 2016.

[34] X. Wang *et al.*, "WSPC-MATERIALS FOR SUSTAINABLE ENERGY-Reprint Volume Book-Trim Size:-11in x 8.5in A metal-free polymeric photocatalyst for hydrogen production from water under visible light," vol. 8, no. January, pp. 271–275, 2010.

[35] B. V. Lotsch *et al.*, "Unmasking melon by a complementary approach employing electron diffraction, solid-state NMR spectroscopy, and theoretical calculations - Structural characterization of a carbon nitride polymer," *Chem. - A Eur. J.*, vol. 13, no. 17, pp. 4969–4980, 2007.

[36] A. Thomas *et al.*, "Graphitic carbon nitride materials: Variation of structure and morphology and their use as metal-free catalysts," *J. Mater. Chem.*, vol. 18, no. 41, pp. 4893–4908, 2008.

[37] X. Zhang, X. Xie, H. Wang, J. Zhang, B. Pan, and Y. Xie, "Enhanced photoresponsive ultrathin graphitic-phase C_3N_4 nanosheets for bioimaging," *J. Am. Chem. Soc.*, vol. 135, no. 1, pp. 18–21, 2013.

[38] W.-J. Ong, L.-L. Tan, Y. H. Ng, S.-T. Yong, and S.-P. Chai, "Graphitic Carbon Nitride (g-C_3N_4)-Based Photocatalysts for Artificial Photosynthesis and Environmental Remediation: Are We a Step Closer To Achieving Sustainability?," *Chem. Rev.*, vol. 116, no. 12, pp. 7159–7329, Jun. 2016.

[39] W. S. Hummers and R. E. Offeman, "Preparation of Graphitic Oxide," *J. Am. Chem. Soc.*, vol. 80, no. 6, pp. 1339–1339, Mar. 1958.

[40] J. Zhang, Y. Chen, and X. Wang, "Two-dimensional covalent carbon nitride nanosheets: Synthesis, functionalization, and applications," *Energy Environ. Sci.*, vol. 8, no. 11, pp. 3092–3108, 2015.

[41] P. Niu, L. Zhang, G. Liu, and H.-M. Cheng, "Graphene-Like Carbon Nitride Nanosheets for Improved Photocatalytic Activities," *Adv. Funct. Mater.*, vol. 22, no. 22, pp. 4763–4770, Nov. 2012.

[42] Q. Lin, L. Li, S. Liang, M. Liu, J. Bi, and L. Wu, "Efficient synthesis of monolayer carbon nitride 2D nanosheet with tunable concentration and enhanced visible-light photocatalytic activities," *Appl. Catal. B Environ.*, vol. 163, pp. 135–142, 2015.

[43] J. Xu, L. Zhang, R. Shi, and Y. Zhu, "Chemical exfoliation of graphitic carbon nitride for efficient heterogeneous photocatalysis," *J. Mater. Chem. A*, vol. 1, no. 46, pp. 14766–14772, 2013.

[44] T. Y. Ma, Y. Tang, S. Dai, and S. Z. Qiao, "Proton-functionalized two-dimensional graphitic carbon nitride nanosheet: An excellent metal-/label-free biosensing platform," *Small*, vol. 10, no. 12, pp. 2382–2389, 2014.

[45] Y. Wang, X. Wang, and M. Antonietti, "Polymeric graphitic carbon nitride as a heterogeneous organocatalyst: From photochemistry to multipurpose catalysis to

sustainable chemistry," *Angew. Chemie - Int. Ed.*, vol. 51, no. 1, pp. 68–89, 2012.

[46] N. Meng, J. Ren, Y. Liu, Y. Huang, T. Petit, and B. Zhang, "Engineering oxygen-containing and amino groups into two-dimensional atomically-thin porous polymeric carbon nitrogen for enhanced photocatalytic hydrogen production," *Energy Environ. Sci.*, vol. 11, no. 3, pp. 566–571, 2018.

[47] M. R. Hoffmann, S. T. Martin, W. Choi, and D. W. Bahnemann, "Environmental Applications of Semiconductor Photocatalysis," *Chem. Rev.*, vol. 95, no. 1, pp. 69–96, Jan. 1995.

[48] R. Hoffmann, "How Chemistry and Physics Meet in the Solid State," *Angew. Chemie Int. Ed. English*, vol. 26, no. 9, pp. 846–878, Sep. 1987.

[49] H. L. Tan, F. F. Abdi, and Y. H. Ng, "Heterogeneous photocatalysts: An overview of classic and modern approaches for optical, electronic, and charge dynamics evaluation," *Chem. Soc. Rev.*, vol. 48, no. 5, pp. 1255–1271, 2019.

[50] Akira Fujishima and Kenichi Honda, "Electrochemical Photolysis of Water at a Semiconductor Electrode One and Two-dimensional Structure of Alpha-Helix and Beta-Sheet Forms of Poly (L-Alanine) shown by Specific Heat Measurements at Low Temperatures (1 . 5-20 K)," *Nature*, vol. 238, no. March, pp. 37–38, 1972.

[51] A. J. Bard, "Design of semiconductor photoelectrochemical systems for solar energy conversion," *J. Phys. Chem.*, vol. 86, no. 2, pp. 172–177, 1982.

[52] M. Rafique *et al.*, "A Comprehensive Study on Methods and Materials for Photocatalytic Water Splitting and Hydrogen Production as a Renewable Energy Resource," *J. Inorg. Organomet. Polym. Mater.*, vol. 30, no. 10, pp. 3837–3861, Oct. 2020.

[53] X. Chen, S. Shen, L. Guo, and S. S. Mao, "Semiconductor-based photocatalytic hydrogen generation," *Chem. Rev.*, vol. 110, no. 11, pp. 6503–6570, 2010.

[54] M. A. Bin Adnan, K. Arifin, L. J. Minggu, and M. B. Kassim, "Titanate-based perovskites for photochemical and photoelectrochemical water splitting applications: A review," *Int. J. Hydrogen Energy*, vol. 43, no. 52, pp. 23209–23220, 2018.

[55] R. C. Pawar, S. Kang, J. H. Park, J. H. Kim, S. Ahn, and C. S. Lee, "Evaluation of a multi-dimensional hybrid photocatalyst for enrichment of H2 evolution and elimination of dye/non-dye pollutants," *Catal. Sci. Technol.*, vol. 7, no. 12, pp. 2579–2590, 2017.

[56] Z. Huang, X. Zeng, K. Li, S. Gao, Q. Wang, and J. Lu, "Z-Scheme NiTiO3/g-C3N4 Heterojunctions with Enhanced Photoelectrochemical and Photocatalytic Performances under Visible LED Light Irradiation," *ACS Appl. Mater. Interfaces*, vol. 9, no. 47, pp. 41120–41125, 2017.

[57] T. T. Pham and E. W. Shin, "Influence of g-C3N4 Precursors in g-C3N4/NiTiO3 Composites on Photocatalytic Behavior and the Interconnection between g-C3N4 and NiTiO3," *Langmuir*, vol. 34, no. 44, pp. 13144–13154, 2018.

[58] T. T. Pham and E. W. Shin, "Thermal formation effect of g-C 3 N 4 structure on the visible light driven photocatalysis of g-C 3 N 4 /NiTiO 3 Z-scheme composite photocatalysts," *Appl. Surf. Sci.*, vol. 447, pp. 757–766, 2018.

[59] Y. Zeng *et al.*, "Fabrication of high-activity hybrid NiTiO3/g-C3N4 heterostructured photocatalysts for water splitting to enhanced hydrogen production," *Ceram. Int.*,

vol. 42, no. 10, pp. 12297–12305, Aug. 2016.

[60]   Q. Wang, Q. Guo, L. Wang, and B. Li, "The flux growth of single-crystalline CoTiO3 polyhedral particles and improved visible-light photocatalytic activity of heterostructured CoTiO3/g-C3N4 composites," *Dalt. Trans.*, vol. 45, no. 44, pp. 17748–17758, 2016.

[61]   L. Zhou, S. Zhang, J. Cheng, L. Zhang, and Z. Zeng, "Optical absorptions of nanoscaled CoTiO3 and NiTiO3," *Mater. Sci. Eng. B*, vol. 49, no. 2, pp. 117–122, Sep. 1997.

Appendix

Figure A1-A2. *Parametric study of the synthetic procedure for MgTiO₃.*
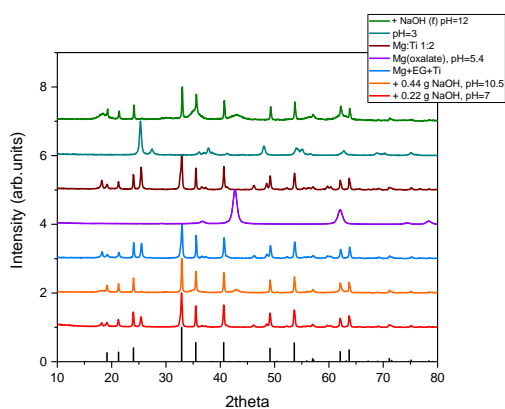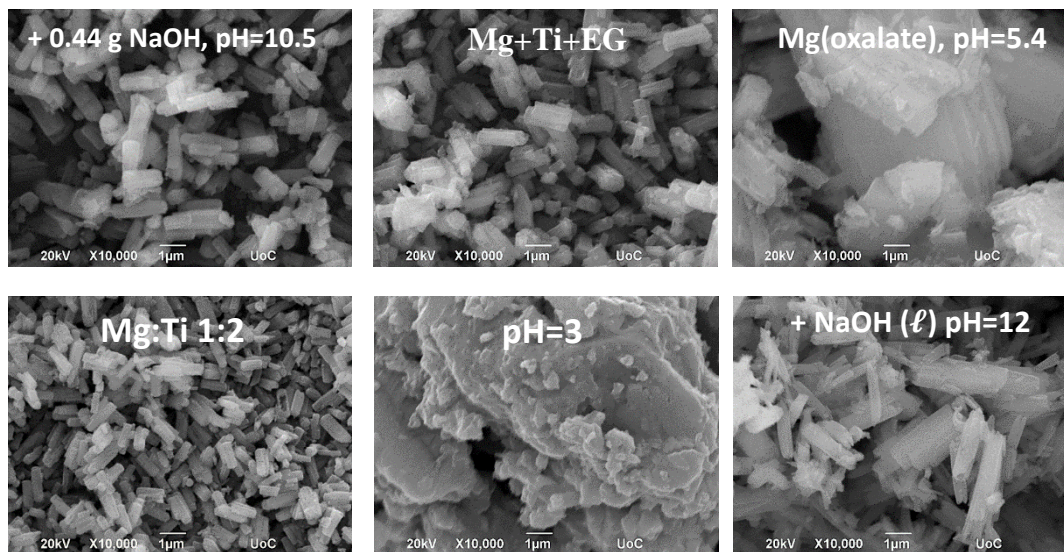
powder	Atomic % (Mg:Ti)
a	1:1
b	1:1
c	99:1
d	1:1
e	2:98
f	1:1
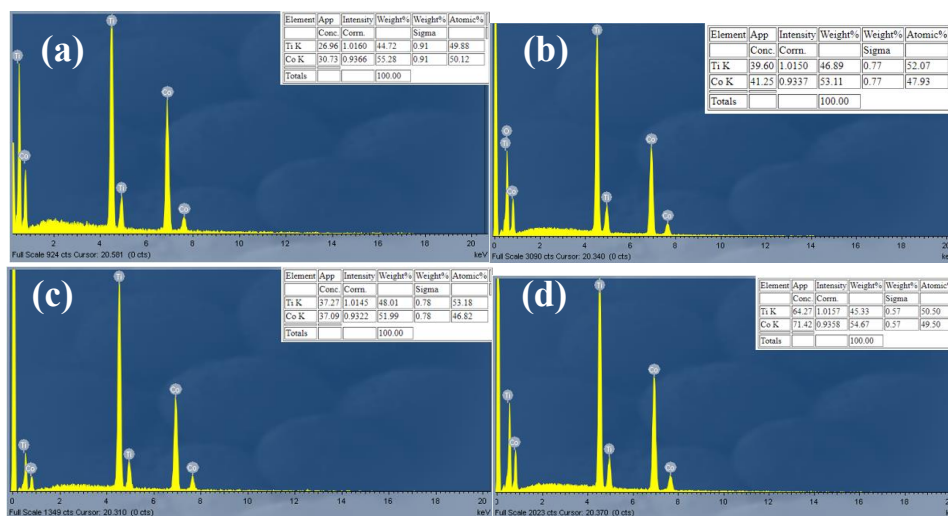
Figure A3. *EDS spectrum of cobalt titanate before annealing, annealed at 400 °C, 600 °C and 800 °C.*
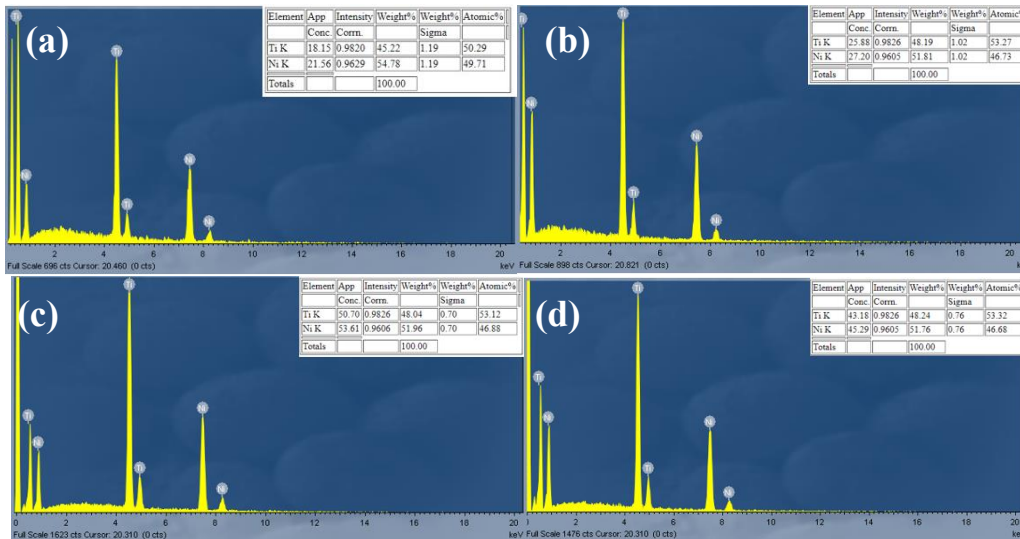
Figure A4. *EDS spectrum of nickel titanate before annealing, annealed at 400 ºC, 600 ºC and 800 ºC.*
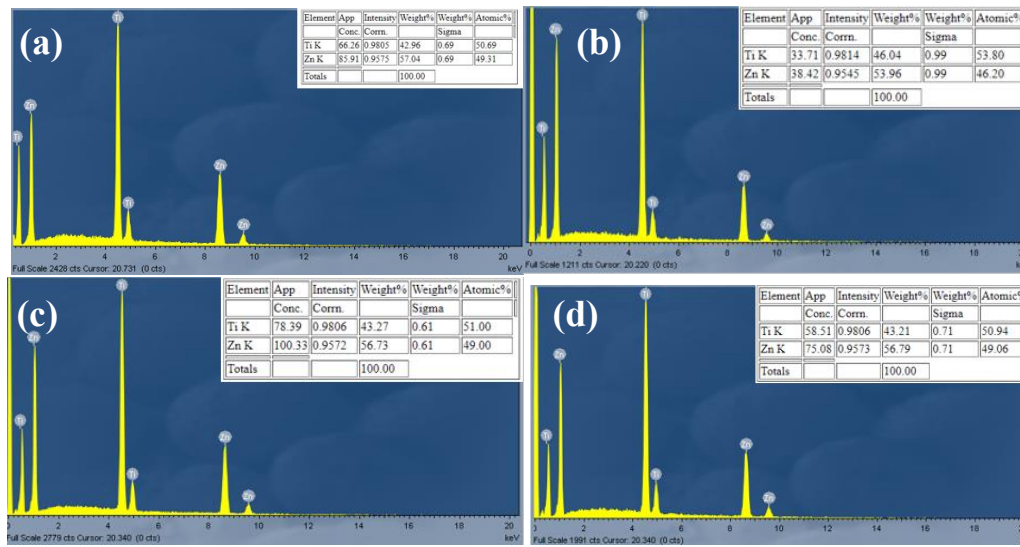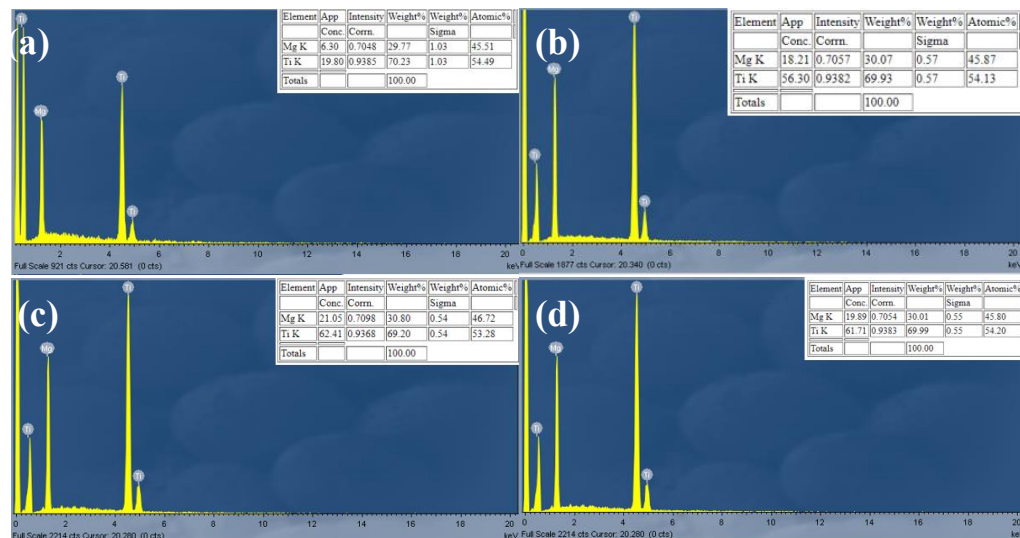

Figure A5. *EDS spectrum of zinc titanate before annealing, annealed at 400 ºC, 600 ºC and 800 ºC.*
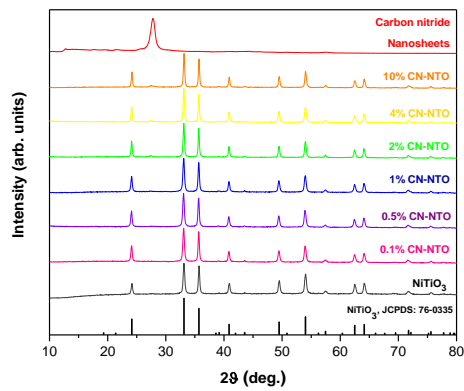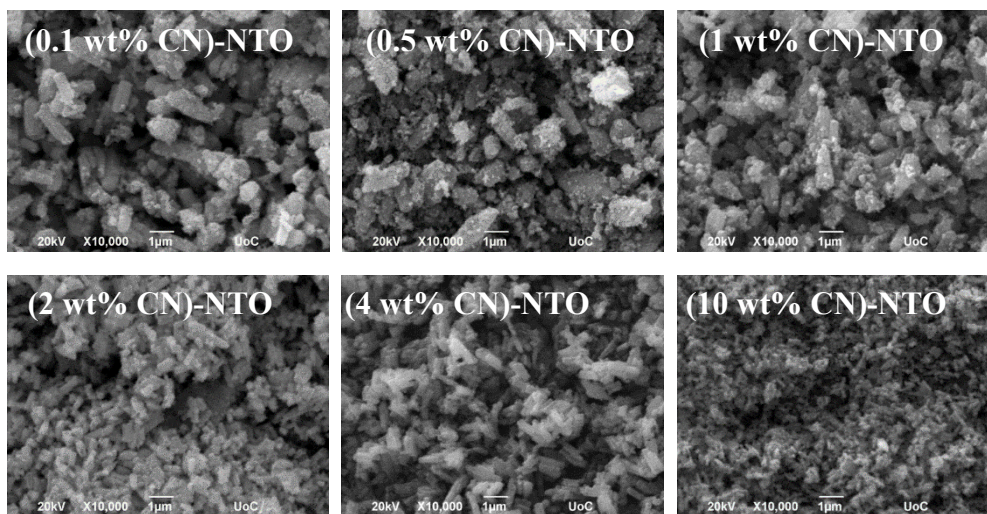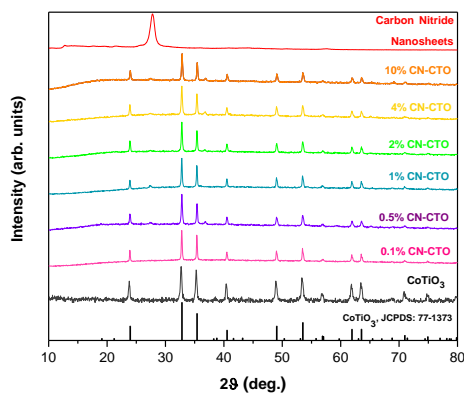

Figure A6. *EDS spectrum of magnesium titanate before annealing, annealed at 400 ºC, 600 ºC and 800 ºC.*

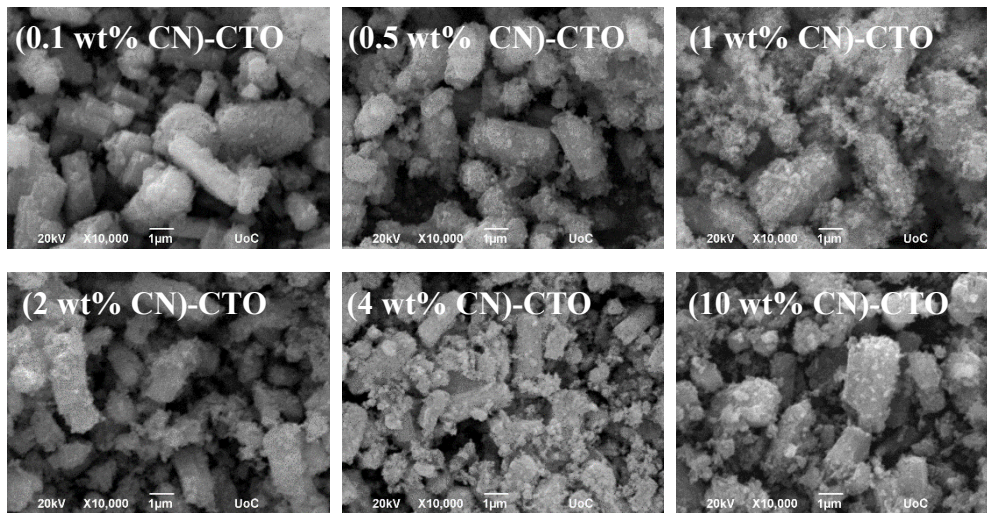***Figure A7.*** *X-ray diffraction pattern of combinations of NiTiO₃ combined with CNNs.*

Figure A8. *SEM pictures of NiTiO₃ combined with CNNs at high magnification.*

Figure A9. *X-ray diffraction pattern of CoTiO₃ combined with CNNs at different concentrations.*

Figure A10. *SEM pictures of CoTiO₃ combined with CNNs at high magnification.*